ON THE VERGE OF BIOORGANIC AND INORGANIC CHEMISTRY: METALLACARBORANES IN NANOMEDICINE

Adnana Alina Zaulet

TESI DOCTORAL

Programa de Doctorat en Química

Director: Prof. Clara Viñas i Teixidor

Tutor: Josefina Pons Picart

Departament de Química

Facultat de Ciències

2015

*3.1.2. NMR study on water solution at different concentrations of the H^+ and Na^+ salts of mono-iodinated [Co(8-I-1,2-$C_2B_9H_{10}$)(1',2'-$C_2B_9H_{11}$)]$^-$, ([I-**3**]$^-$), and di-iodinated [Co(8-I-1,2-$C_2B_9H_{10}$)$_2$]$^-$, ([I_2-**3**]$^-$)*

Mátel and co-workers[22] reported a method leading to a quantitative conversion of parent [**3**]$^-$ into the corresponding B(8) monoiodate compound [Co(8-I-1,2-$C_2B_9H_{10}$)(1',2'-$C_2B_9H_{11}$)]$^-$, ([I-**3**]$^-$). However, we found that applying this procedure a mixture of the starting compound [**3**]$^-$ and the desired product [I-**3**]$^-$ was obtained. Therefore we slightly modified the reported procedure in order to obtain [I-**3**]$^-$ as a pure compound. Under the new reaction conditions the yield increased from 84 % in the reported procedure to 95%, and the work up has been shortened. Also, the cesium salt of [Co(8-I-1,2-$C_2B_9H_{10}$)$_2$]$^-$, Cs[I_2-**3**], was prepared by a modification of the original synthesis by Mátel et al.[22] employing ICl instead of I_2. The procedure is much more simple providing a rapid and reliable synthesis of multigram quantities of [I_2-**3**]$^-$ in an overall yield of 98% with an easy purification step (Scheme 3.1).[4b]

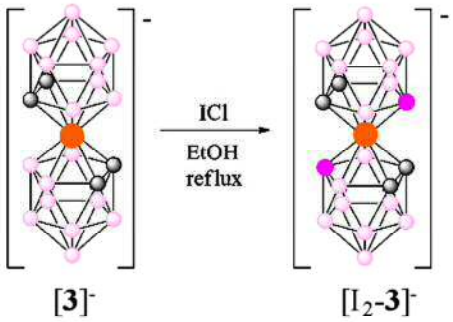

Scheme 3.1. Procedure of the synthesis of Cs[I_2-**3**].

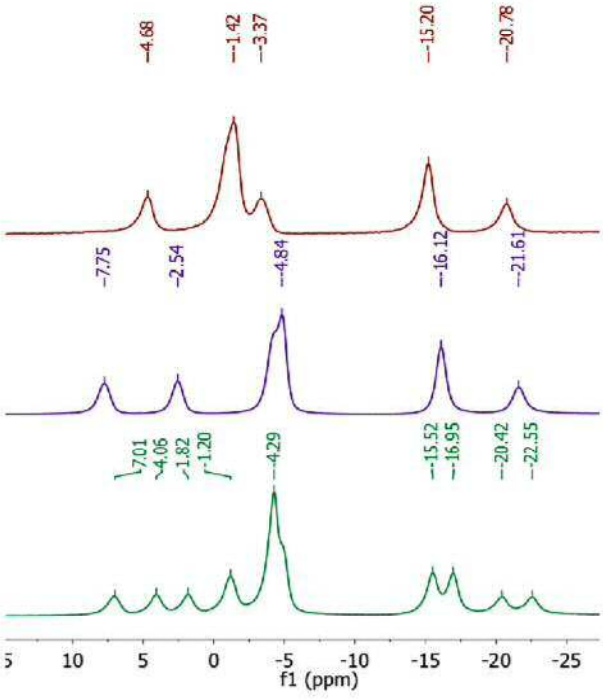

Figure 3.8. $^{11}B\{^1H\}$-NMR spectra of [I_2-**3**]$^-$ (in red), [**3**]$^-$ (in blue), [I-**3**]$^-$ (in green).

Figure 3.8 displays the $^{11}B\{^1H\}$-NMR spectra in acetone of the cesium salt of the parent [**3**]$^-$ (in the center) and the mono-iodinated [3,3'-Co(8-I-1,2-$C_2B_9H_{10}$)(1',2'-$C_2B_9H_{11}$)]$^-$ and di-iodinate [3,3'-Co(8-I-1,2-$C_2B_9H_{10}$)$_2$]$^-$ derivatives, [I-**3**]$^-$ and [I_2-**3**]$^-$, at the bottom and at the top, respectively, noticing asymmetry in [I-**3**]$^-$.

The ^{11}B-NMR spectrum of monosubstituted of Cs[**3**] is the result of the addition of the two individual halves, as schematised in Figure 3.9. According to it, the $^{11}B\{^1H\}$-NMR of the monosubstituted Cs[I-**3**] is the addition of the $^{11}B\{^1H\}$-NMR spectrum of the parent Cs[**3**] plus the $^{11}B\{^1H\}$-NMR spectrum of disubstituted Cs[I_2-**3**]. As shown in Figure 3.8, the spectrum of Cs[**3**] (in the middle) displays resonances at ppm, 7.7(2), 2.5(2), -4.8(8), -16.1(4) and -21.6(2) and the spectrum of Cs[I_2-**3**] (at the top) displays resonances at ppm 4.7(2), -1.4(8), -3.4(2), -15.2(4) and -20.8(2). The spectrum of Cs[I-**3**] (at the bottom) should then be very close to 7.7(1), 4.7(1), 2.5(1), -1.4(4), -4.8(4), -3.4(1), -15.2(2), -16.1(2), -20.8(1), and -21.6(1) that corresponds to the addition of the two different half valves. The experimental spectrum of Cs[I-**3**] consists of bands at 7.0(1), 4.1(1), 1.8(1), 1.2(2), -4.3(7), -15.5(2), -17.0(2), -20.4(1), and -22.6(1). We have tested this method with other available examples and it works extremely well.[4b,45] This is therefore a remarkable tool to assist in the structural elucidation of derivatives of [**3**]$^-$ mainly when other techniques like COSY, GIAO are not applicable.

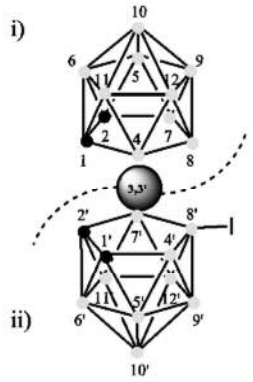

Figure 3.9. The $^{11}B\{^1H\}$-NMR spectrum of [3,3'-M(8-I-1,2-$C_2B_9H_{10}$)(1',2'-$C_2B_9H_{11}$)]$^-$ is the result of the addition of the two individual halves: i) + ii). Vertexes numbering for [3,3'-M(8-$(OCH_2CH_2)_2$R-1,2-$C_2B_9H_{10}$)(1',2'-$C_2B_9H_{11}$)]$^-$.

3.1.2.a.-NMR study in water solution at different concentrations of the H^+ and Na^+ salts of mono-iodinated [I-3]$^-$ complex

Figure 3.10 shows the $^{11}B\{^1H\}$-NMR study in D_2O of the H[I-**3**], Na[I-**3**] at different concentrations: 5 (in red), 10 (in light green), 15 (in green), 20 (in light blue), 25 (in blue) and 30 mM (in purple) were carried out. From this study, one may conclude that the monoiodinated species [I-**3**]$^-$ produces aggregates either from its H^+ or Na^+ salt at concentration higher that 15 mM.

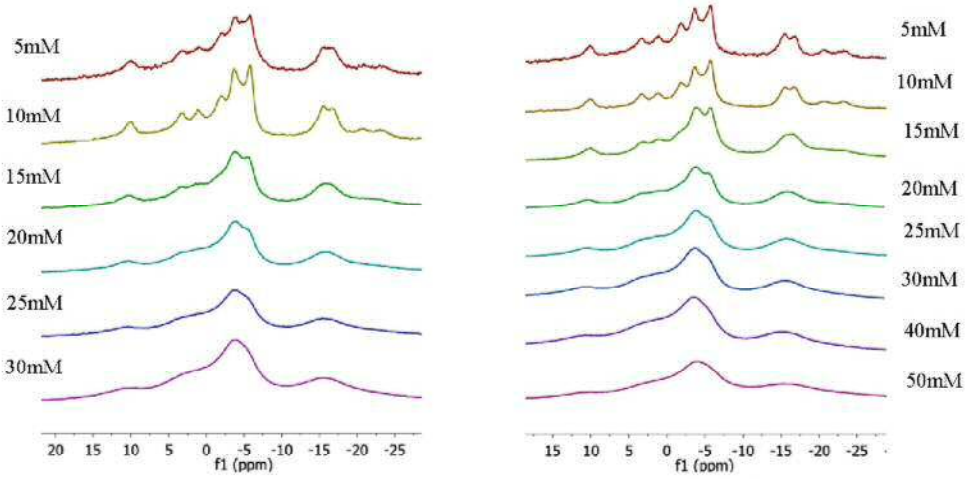

H[I-**3**] Na[I-**3**]

Figure 3.10. $^{11}B\{^1H\}$-NMR studies in D_2O of the H[I-**3**], Na[I-**3**] at different concentrations.

3.1.2.b.-NMR study on water solution at different concentrations of the H^+ and Na^+ salts of di-iodinated $[Co(8\text{-}I\text{-}1,2\text{-}C_2B_9H_{10})_2]^-$, $[I_2\text{-}3]^-$

Following with the previous studies, the $^{11}B\{^1H\}$- and $^1H\{^{11}B\}$-NMR spectra in D_2O of the H^+ and Na^+ salts of the disubstituted $[I_2\text{-}3]^-$ species were also run at different concentrations: 2.5, 5, 10, 20, 30 and 60 mM (Figure 3.11).

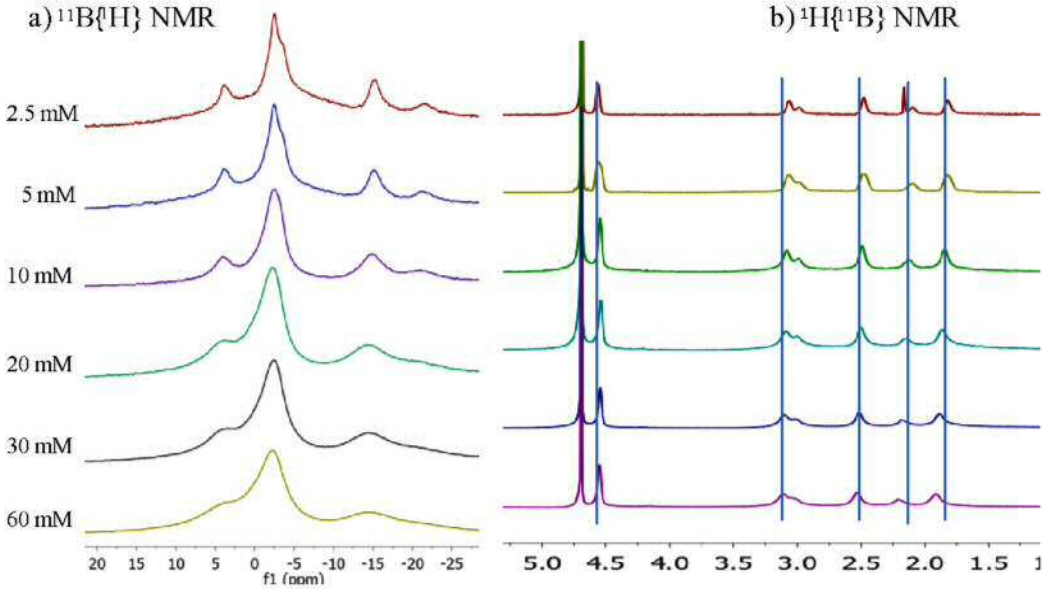

Figure 3.11. $^{11}B\{^1H\}$- and $^1H\{^{11}B\}$-NMR spectra in D_2O of Na[I_2-**3**] at different concentrations.

As shown in Figure 3.12, the solvent and the concentration of the metallacarbonare have an influence on the color of the solutions as it was observed on the NMR spetra.

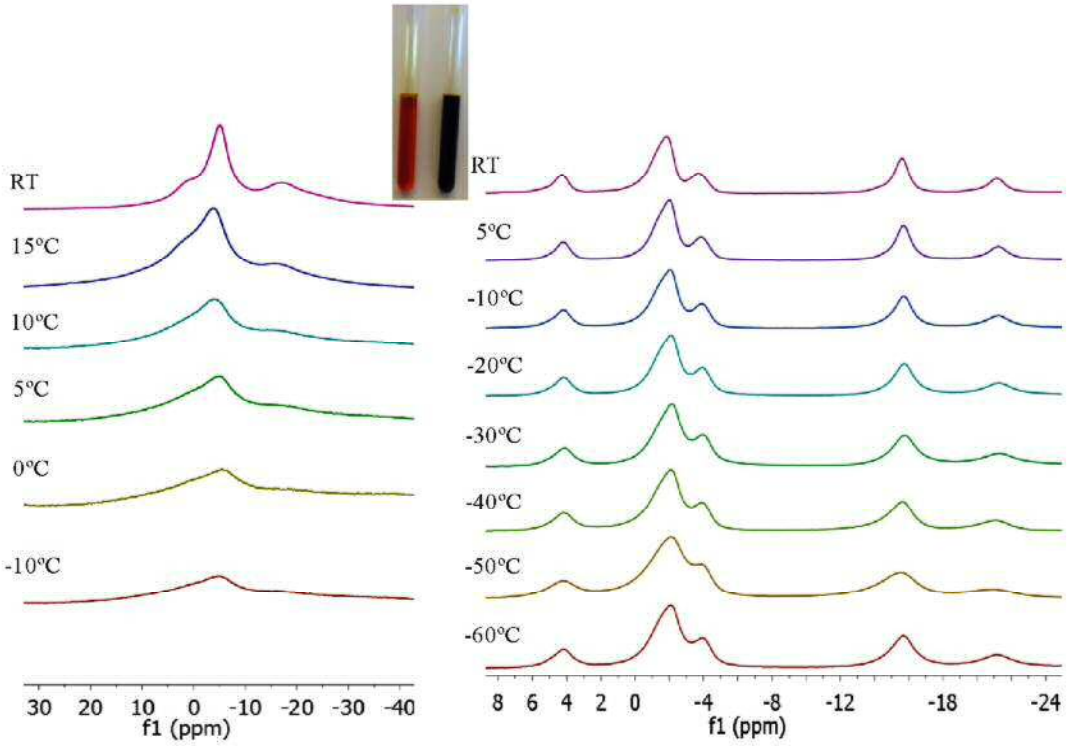

Figure 3.12. Displays the $^{11}B\{^1H\}$-NMR dynamic study of the 0.1 M solutions of the protonated salt of $[I_2\text{-}\mathbf{3}]^-$ in both aqueous (left) and acetone (right) solutions.

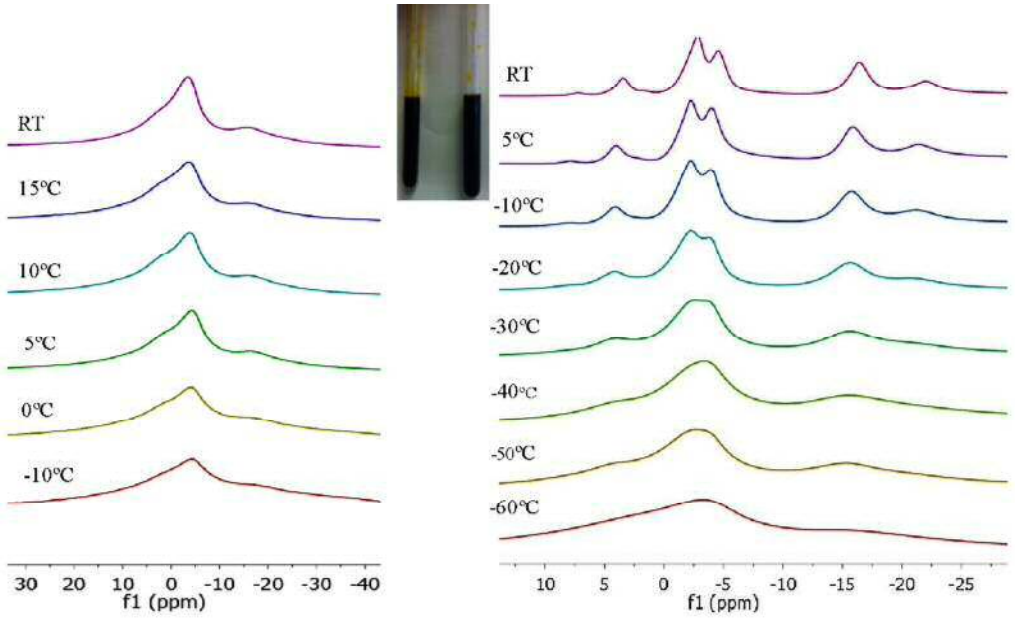

Figure 3.13. Displays the $^{11}B\{^1H\}$-NMR dynamic study of the 1 M solutions of the protonated salt of $[I_2\text{-}\mathbf{3}]^-$ in both aquous (left) and acetone (right) solutions.

From the study of the $^{1}H\{^{11}B\}$-NMR spectra a different concentrations, it can be observed that the chemical shift of the C_c-H vertex remains unaffected while the B-H resonances are slightly up shielded (see Figure 3.11).

The $^{11}B\{^{1}H\}$-NMR dynamic studies of the 0.1 M and 1 M solutions of H[I_2-**3**] salt in aqueous and acetone solutions in the temperature range 20°C - -60°C was done.

As it has been discussed in the previous section, the H[**3**] self-assembles in water by forming isotropic phases: vesicles of monomolecular thickness in diluted regime that turn into small micelles by increasing concentration. In this section, by combining visual observations, dynamic and static light scattering (DLS/SLS), small and wide-angle X-ray scattering (SWAXS), $^{11}B\{^{1}H\}$ NMR spectroscopy (see Figure 3.11 left), polarized optical light microscopy (POM) and freeze-fracture electron microscopy (FF-TEM), several ordered and disordered phases were identified over a large range of temperature and concentration. In the diluted regime, H[I_2-**3**] was found to behave similarly as H[**3**] by forming vesicles with a radius of gyration of around 98.3 nm as determined by DLS/SLS (see Figure 3.15a). At high concentrations above 35%v/v, optical microscopy pictures show birefringence with the presence of Maltese crosses (left side in Figure 3.15b) that are typical of lamellar phases. Applying a soft shear stress, by sliding the microscopy slide cover slip, the system can be easily mechanically aligned over one centimeter square (right side of Figure 3.15b). At temperatures below 20°C and volume fractions above 40%, the SWAXS spectra showed a series of

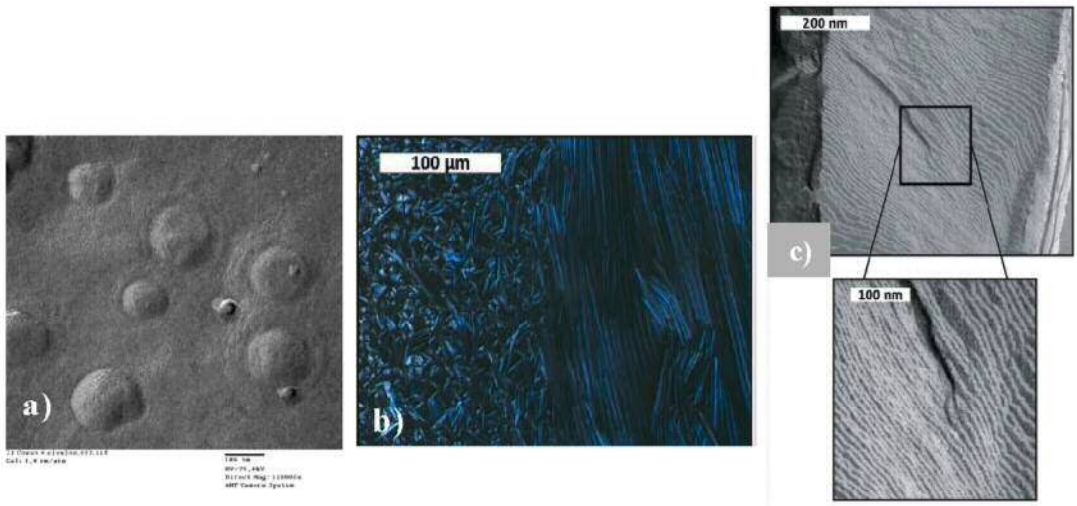

Figure 3.15. a) Vesicles formation b) lyotropic lamellar structure observed by Advanced Microscopy Techniques (AMT); c) shows the freeze-fracture TEM picture of the pure lamellar arrangement with an apparent inter-lamellar distance of roughly 5 nm confirmed by SWAXS.

diffraction peaks which are typical of a lamellar ordering that confirms the microscopy observation (Figure 3.15c displays SWAXS spectrum at 218°K).

Lyotropic lamellar phases are ubiquitous in the high concentration range of binary surfactant/water mixtures. The present study showed that the formation of lamellar phases is not exclusive to alkyl chain based surfactants with a well-defined amphiphilic structure but can also be obtained with metalla-carborane clusters, described previously as theta-shaped amphiphiles. As for classical surfactants the lamellae formed can exist both in the liquid and in the solid states depending on temperature. It was concluded from the 2D molecular arrangement in the lamellae that the formation of intermolecular hydrogen bonds, such as $-C_c\text{-}H^{\delta+}\cdots{}^{\delta-}H\text{-}B\text{-}$, is the driving force in the lamella formation (Figure 3.16).

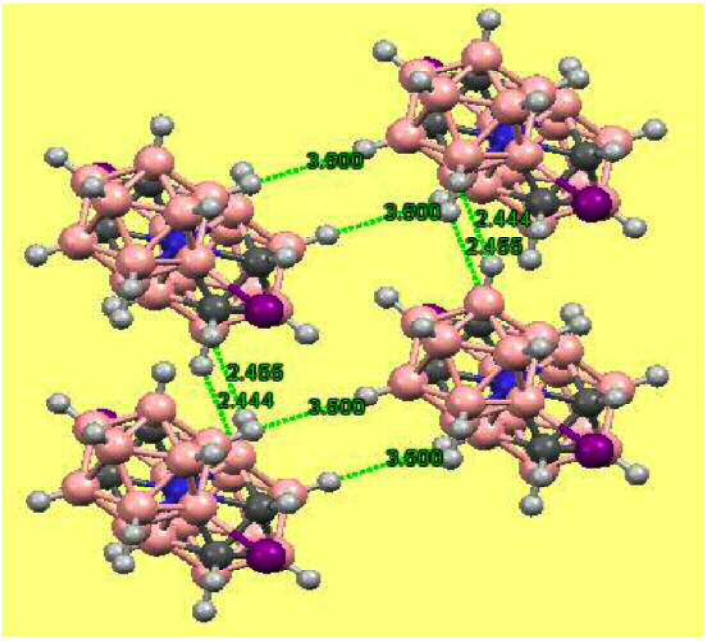

Figure 3.16 A view of the crystal packing of [BEDT-TTF]$_2$[I_2-**3**] (CSD code IHOHAP).[46] Interactions B-H···H-B and C_c-H···I-B are depicted as pale blue dotted lines. White = H, pink = B, grey = C, purple = I.

Compared to the common bilayer structure that originates from the hydrophobic effect, theta-shaped amphiphiles form lamella with a peculiar monomolecular structure reminiscent of lamellar sheets observed in clays. This monomolecular structure also constitutes the wall of the vesicles formed in the diluted regime as it was highlighted in the previous section. Consequently concentration and temperature controlled nano-scale

ordering of planar organic-inorganic hybrid sheets are reached through a self-assembly process.

We can thus propose a 2D lattice of the lamellae, as shown in Figure 3.16, which is in good agreement with the molecular distances with one $[I_2\text{-}\mathbf{3}]^-$ ion per lattice. In this structure it was considered that $[I_2\text{-}\mathbf{3}]^-$ ions present a two-fold symmetry with the two iodine atoms in *trans* position, as shown in Figure 3.17, which represents the most stable rotamer, that is, transoid, as supported by the crystal structures (codes DEXPIF, IHOHAP, IHOHET and IHOHIX) in the Cambridge Structural Database. The 2D arrangement shows that $[I_2\text{-}\mathbf{3}]^-$ ions are not in close contact but are separated by a distance of 3.5 that may be due to the presence of intermolecular dihydrogen bonds, such as -C-$H^{\delta+}\cdots^{\delta-}$H-B or B-$H^{\delta+}\cdots^{\delta-}$H-B, reducing the energy of the crystal. Such dihydrogen bonds are observed in the solid state for the [BEDT-TTF][I_2-**3**] (CSD code IHOHAP)[46] which has dihydrogen B-$H^{\delta+}\cdots^{\delta-}$H-B bonds of 3.500 Å matching the value found in our case (Figure 3.16). According to the 2D structure, it is then likely that the self assembly process of $[I_2\text{-}\mathbf{3}]^-$ ions in monomolecular lamella relies on a network of such H-bonds while the formation of bilayers with classical surfactants is mainly driven by the hydrophobic effect.

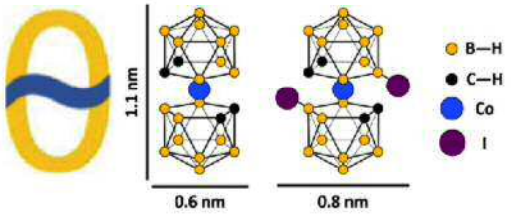

Figure 3.17. Chemical structure of the amphiphilic ion, $[3]^-$ (left), and its diiodinated derivative, $[I_2\text{-}\mathbf{3}]$ (right) whose shape is compared to the Greek letter Θ (far left).

The former results show that lyotropic lamellar phases can not only be formed from alkyl-chain-based surfactants with a well-defined amphiphilic structure but they can also be obtained from metallacarborane clusters, described as θ-shaped amphiphiles. The lamellae formed are unique as they have a monomolecular thickness.

This information on the intermolecular forces involved in the self-assembly of $[\mathbf{3}]^-$ derivatives in water is essential for a rational design for their applications in many different fields, such as in the reprocessing of spent nuclear fuel,[28b] in analytical chemistry as main component in ion-selective electrodes,[47] in solar cells design as fast redox shuttle,[48] in medicine as promising building block for drug design[49] or in boron-neutron capture therapy.[50] The organic–inorganic hybrid lamellar phases studied could have potential applications as new liquid crystal systems for display or memory storage if the cobalt center can be replaced with a magnetic atom, such as iron. The tunable

oxidation state of the theta-shaped amphiphile metal[51] could also be used to design active nano-materials for sensing and for photonic applications.

3.1.3.- Study of the H^+ and Na^+ salts of [3,3'-Fe(1,2-$C_2B_9H_{11}$)$_2$]$^-$, [4]$^-$

To study the behavior of the sodium salt of the anion [**4**]$^-$ in aqueous solution as a function of the concentration, $^{11}B\{^1H\}$- and $^1H\{^{11}B\}$-NMR spectra were run. As shown in Figure 3.19 a, the resonances corresponding to the B vertices in the $^{11}B\{^1H\}$-NMR spectra remain unaltered from 5 to 20 mM but, they are slightly shifted to a higher field at concentrations higher than 30 mM. While the influence of the concentration on the chemical shift of the hydrogen atoms bonded to the Boron vertices is really clear as show in Figure 3.19b. The chemical shift at 44.13 ppm that was assigned to the C_c-H of the Na[**4**] species moves upfield being the difference from 5 mM to 100 mM of 10.51 ppm. The upfield shifting of all resonances, C_c-H and B-H vertices, when increasing the concentration is noticeable and remarkable. If we compare the effect of the concentration in the $^1H\{^{11}B\}$-NMR of Na[**4**] (Figure 3.19b) and Na[**3**] (Figure 3.7) species, we observe that the difference is 9.16 ppm for Na[**4**] and 0.13 ppm for Na[**3**] when concentration increases from 5 mM to 60 Mm in both cases. Because an examination of the Cambridge Structural Database [18a, 52] showed just seven X-ray structures of the [3,3'-Fe(1,2-$C_2B_9H_{11}$)$_2$]$^-$ framework (HAPCUW, [53] HIMKUJ, [54] KWJOP, [55] LINFAQ, [56] QATPEI, [57] WEKJEB [58] and YEDVUY [59]) but no one has a proton or alkaline or alkaline-earth cation.

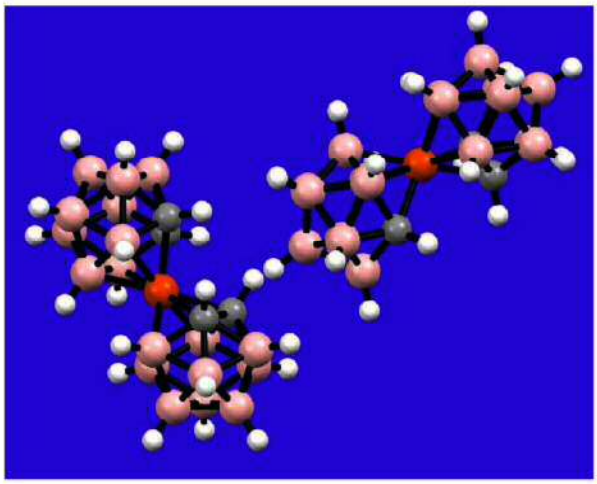

Figure 3.18. Crystal structure of H[**4**].

So, in this thesis, great effort was done on growing good crystals of [**4**]$^-$. We were able to obtained suitable crystals for X-ray diffraction of the H[**4**] from a benzene solution. The crystal structure possesses two different molecules. Each one is involved in a contact shorter than 0.4 Å the sum of the vdV radii that corresponds to C_c-H···H-B. In one of them three more C_c-H···H-B contacts shorter than 0.3 Å the sum of the vdV radii

are observed; that it means all four C_c-H vertexes are involved in C_c-H···H-B weak interactions. Whilst that only two C_c-H vertexes from the other molecule, one from each $[C_2B_9H_{12}]^-$ ligand, are involved in C_c- H···H-B contacts shorter than 0.3 Å.

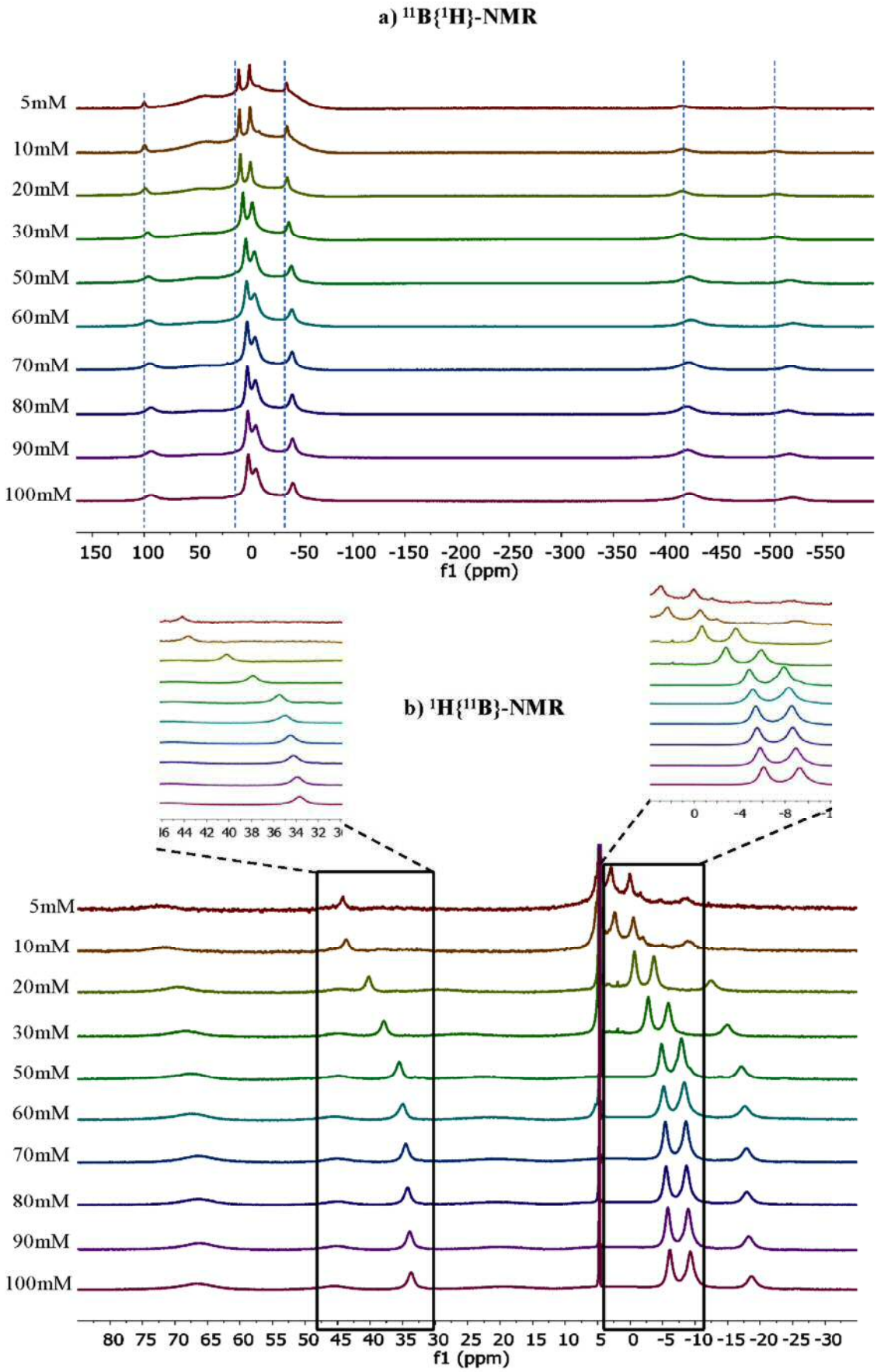

Figure 3.19. $^{11}B\{^{1}H\}$- and $^{1}H\{^{11}B\}$-NMR spectra (a and b, respectively) in D_2O of Na[**4**] at different concentrations.

4.1.- Reduction of Co(III) and Fe(III) to Co(II) and Fe(II) to produce the Na_2[3,3'-Co(8,9,10,12-I_4-1,2-$C_2B_9H_7)_2$] and Na_2[3,3'-Fe(1,2-$C_2B_9H_{11})_2$] compounds

4.1.1.- Co(III) to Co(II):

The $E_{½}$ value of the platform [**3**]$^-$/ [**3**]$^{2-}$ is -1.80 *vs* Fc^+/Fc,[3,22,60] while the redox potential of [3,3'-Co(8,9,10,12-I_4-1,2-*closo*-$C_2B_9H_7)_2$]$^-$ / [3,3'-Co(8,9,10,12-I_4-1,2-*closo*-$C_2B_9H_7)_2$]$^{2-}$ ([I_8-**3**]$^-$/[I_8-**3**]$^{2-}$) pair is -0.68 V *vs.* Fc^+/Fc.[61] We wanted to learn more on the stability of both members of this uncommon redox couple [I_8-**3**]$^-$/[I_8-**3**]$^{2-}$ with a practical $E_{½}$ value. In [**3**]$^-$, the Co is Co^{3+}, and as the dicarbollide is a high field ligand, the 6 electrons d are paired, thus [**3**]$^-$ is a diamagnetic species. In [**3**]$^{2-}$, there are 7 electrons d, and a paramagnetic species is expected. For [**3**]$^-$, the independent oxidized and reduced species would be difficult to be observed, indeed the reduced form has never been reported nor isolated, but in [I_8-**3**]$^-$ the chances to observe both redox partners should be much higher. Furthermore, tests on the stability of both forms, oxidized and reduced, in not highly strict anaerobic conditions would be a good indication of possible applications of these complexes. In a typical reaction the Na^+ salt of [I_8-**3**]$^-$ was dissolved in deoxygenated water and mixed with $NaBH_4$. Immediately the color of the solution turned from light orange to dark red. Progress of the reaction was followed by NMR analysis directly from the crude and the $^{11}B\{^1H\}$-NMR spectrum gave four well defined NMR resonances with intensities 2:6:4:6 in a wide field range (+28 / -95 ppm), clearly suggesting that the generated species was paramagnetic. Following oxidation by air, the sample returned to the original Co^{3+} color and its $^{11}B\{^1H\}$-NMR spectrum to the expected range (-2 / -20 ppm). The $^{11}B\{^1H\}$-NMR for [I_8-**3**]$^-$ evidences the diamagnetic nature of the compound. Conversely the ^{11}B-NMR of [I_8-**3**]$^{2-}$ expands significantly evidencing the paramagnetic nature of the reduced form. This is the first reported $^{11}B\{^1H\}$-NMR spectrum of one derivative of the cobaltabis(dicarbollide) platform proving the stability of the reduced species. To detect the presence of Co^{2+}, the EPR spectrum of a 33 mM solution of [I_8-**3**]$^{2-}$ in H_2O was recorded at 130K showing a g= 2,021. With these results in hand other tests were done to isolate [I_8-**3**]$^{2-}$.[62] The final compound was collected as a dark brown. The further $^{11}B\{^1H\}$-NMR analysis showed that it was not altered during the purification process.

Moreover, the stability in both air and inert gas (N_2 and Ar) conditions was also checked. The $[I_8\text{-}\mathbf{3}]^{2-}$ species in solid state was perfectly air-stable for 7 days, while under inert conditions its stability increased to more than 1 month. The water solution of the $[I_8\text{-}\mathbf{3}]^{2-}$ species was stable for several hours in air. After some day, some re-oxidation was observed.

4.1.2.- Fe(III) to Fe(II):

Similar to $[\mathbf{3}]^-$, the $[\mathbf{4}]^-$ species is also reversibly electroactive, but this platform has $E_{1/2} = -0.78$ V *vs* Fc^+/Fc,[35,31a] which is very similar to that found for the octa-iodinated derivative $[I_8\text{-}\mathbf{3}]^-$.[61,62] The objective of this section was to see how the presence of halogen atoms bonded to the $[\mathbf{4}]^-$ platform would affect the $E_{1/2}$ of the Fe(III) to Fe(II). The first step was to design a proper way to reduce the Fe(III) species.

Two ways were used for the synthesis of the reduced Fe(II) species, $[\mathbf{4}]^{2-}$ depending of the cation of the starting species $[\mathbf{4}]^-$ one.

a) Synthesis of $[NMe_4][Na][\mathbf{4}]$: to a solution of $[NMe_4][\mathbf{4}]$ in dry Glyme under nitrogen atmosphere, $NaBH_4$ was added in solid. After some minutes of stirring, a pink color appears that indicate the reduction of Fe(III) to Fe(II). The reduced form was checked by ^{11}B-NMR.

b) Synthesis of $Na_2[\mathbf{4}]$: to a deoxygenated aqueous solution of $Na[\mathbf{4}]$, $NaBH_4$ was added in solid. After 20 min of stirring the dark red solution turn to pink solution.

$Na_2[Cl_6\text{-}\mathbf{4}]$ has been obtained using the procedure b; the color solution changed from green to pink.

As it was written in the section 2.1.3.a, the two species $[I_8\text{-}\mathbf{4}]^-$ and $[I_8\text{-}\mathbf{4}]^{2-}$ were obtained from the synthesis reaction and it is easily observed the widening of the spectrum of paramagnetic $Cs_2[I_8\text{-}\mathbf{4}]$.

Both $^{11}B\{^1H\}$-NMR for $[I_8\text{-}\mathbf{4}]^-$ (in red) and $[I_8\text{-}\mathbf{4}]^{2-}$ (in black) are shown in Figure 4.1.

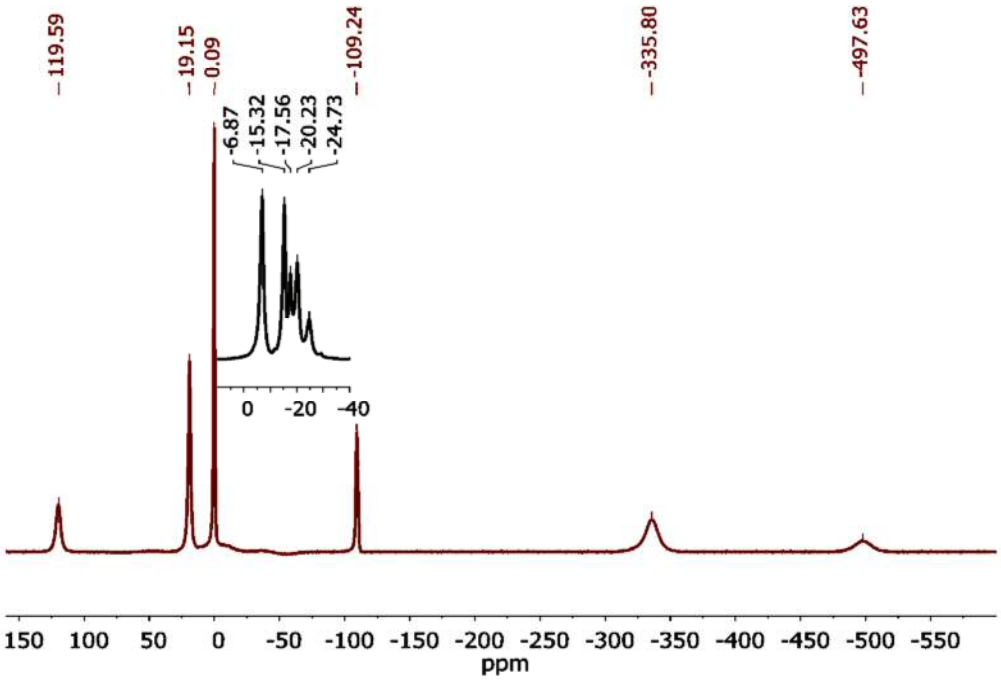

Figure 4.1. Comparison between the $^{11}B\{^{1}H\}$-NMR spectra of the paramagnetic Fe(III) and the diamagnetic Fe(II) species; oxidized $[I_8\text{-}\mathbf{4}]^-$ (in red) and the reduced $[I_8\text{-}\mathbf{4}]^{2-}$ (in black), respectively.

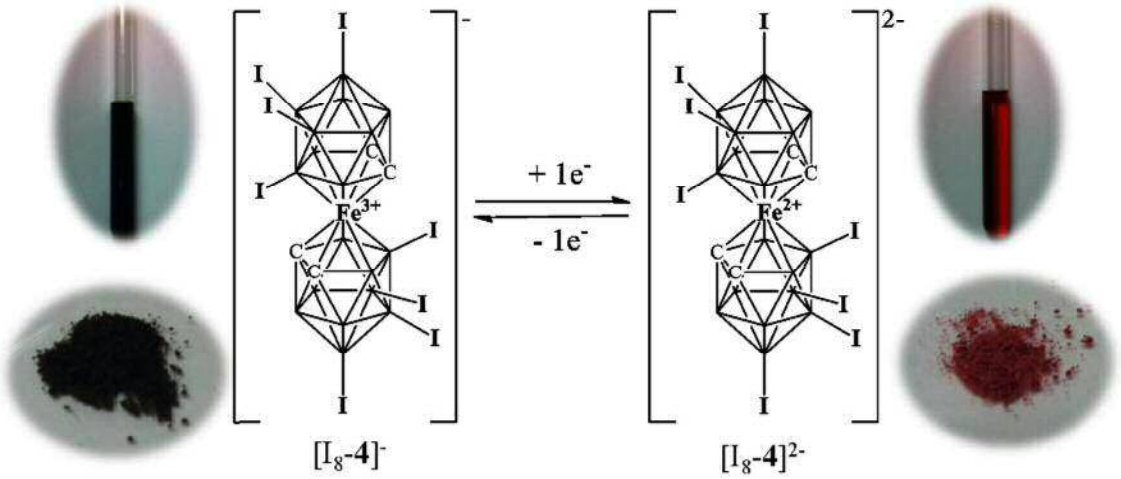

Figure 4.2. Air stability of both compounds: paramagnetic $[I_8\text{-}\mathbf{4}]^-$ in dark green and diamagnetic $[I_8\text{-}\mathbf{4}]^{2-}$ in pink.

As displayed in Figures 4.3, the Fe(III) paramagnetic species presents a weighted average ^{11}B-NMR chemical shift, $\langle\delta(^{11}B)\rangle$, of the order of ca. -124 ppm, at 90 ppm higher frequency than those of related Co(II) paramagnetic metallacarborane (ca. -35 ppm). The same is observed by the two octaiodinated diamagnetic species, $[I_8\text{-}\mathbf{3}]^{2-}$ and

$[I_8\text{-}\mathbf{4}]^-$, (Figures 4.4) and parent species, $[\mathbf{3}]^-$ and $[\mathbf{4}]^{2-}$, (Figure 4.5), being the order of ca. -9 / -15 ppm and -7 / -15 ppm, respectively.

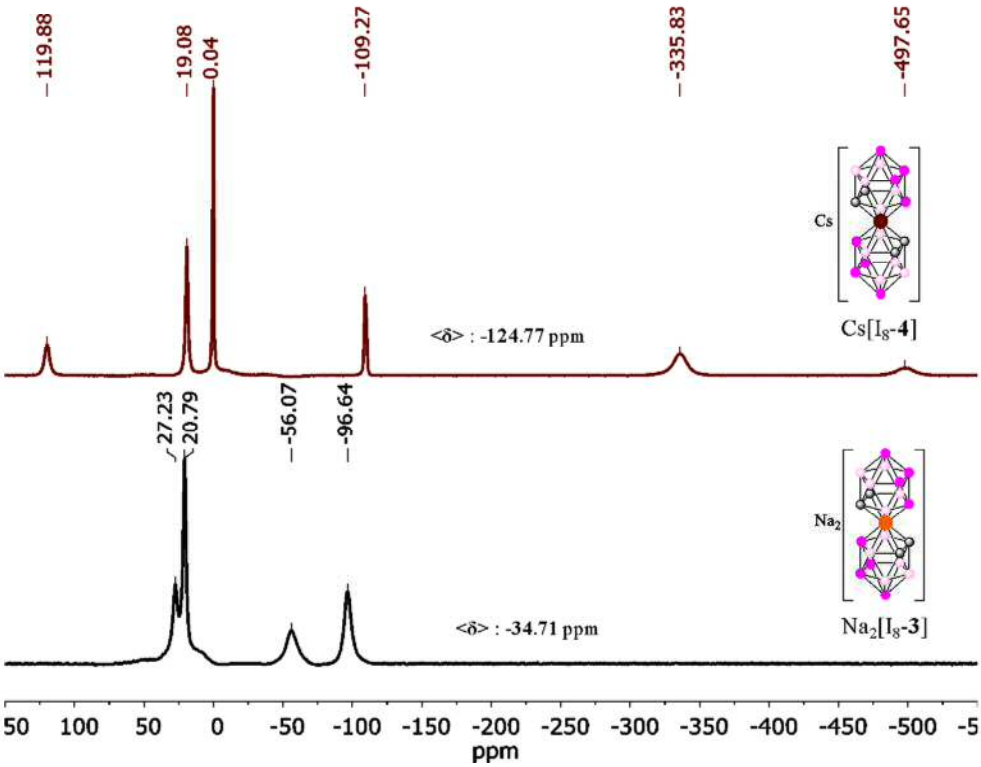

Figure 4.3. $^{11}B\{^1H\}$-NMR spectra in d^6acetone and H_2O of the two paramagnetic species: $Cs[I_8\text{-}\mathbf{4}]$ (in red) and $Na_2[I_8\text{-}\mathbf{3}]$ (in black); oxidized Fe(III) and the reduced Co(II) respectively.

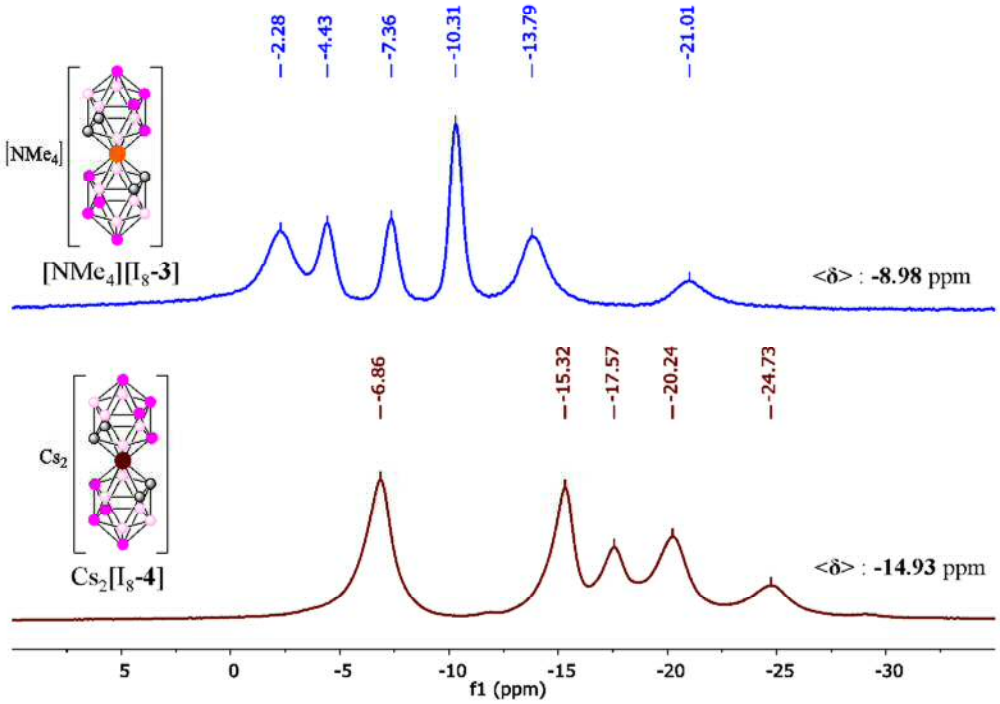

Figure 4.4. $^{11}B\{^{1}H\}$-NMR spectra of the two diamagnetic species: $[NMe_4][I_8$-**3**] species (in blue) and $Cs_2[I_8$-**4**] species (in red); the oxidazed Co(III) and reduced Fe(II), respectively.

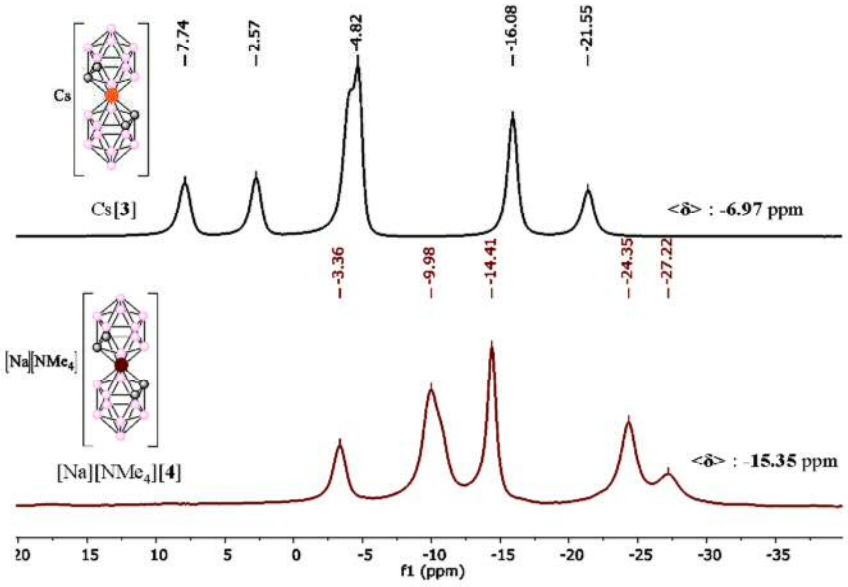

Figure 4.5. $^{11}B\{^{1}H\}$-NMR spectra of the two diamagnetic species: Cs[**3**] species (in black) and [Na][NMe_4][**4**] species (in red); the oxidazed Co(III) and reduced Fe(II), respectively.

5.1.- Electrochemistry

Once several families of anionic methylated and halogenated metallabis(dicarbollide) derivatives have been synthesized, isolated and characterized as it has been presented in the previous sections, the next step was to study the electrochemical properties of all complexes.

The cobaltabisdicarbollide, [3,3'-$Co(C_2B_9H_{11})_2$]$^-$, [**3**]$^-$,[63] is a remarkable anion: it is chemically and thermally stable in a diverse number of situations;[64] it can be substituted at carbon atoms or at boron atoms,[39b] and in the latter ones regioselectively at different sites of each one of the two globes.[65] The central core of this anion, "$Co(C_2B_3)_2$", is very similar to the core of ferrocene (*Fc*), "$Fe(C_5)_2$", thus they bear resemblances in some respects, e.g. the reversible electrochemistry[66] and the high chemical and thermal stability,[39a] but are different in others, such an enhanced protection of the Co in [**3**]$^-$ by a canopy of boron hydrogen atoms,[67] and properties derived from the six additional atoms placed in two further planes from the core (B_5 plane and B_1). These vertexes produce a rich variety of substitution sites, and are responsible for additional physicochemical properties. One of the most obvious differences between [**3**]$^-$, and ferrocene is the charge of [**3**]$^-$, that makes the latter and its congeners to be some of the few examples of metallocene type complexes with a negative charge. Previous work has shown that [**3**]$^-$ can be modified by halogenations,[68, 21,22,25,46] and it is a unique framework in its ability to produce a stepwise modulation of its redox potential by each new B-X (X = halogen) unit added.[29] We recently demonstrated that sequential substitution of B-H by B-X units produces an average $E_{½}$ shift, near 0.13V, to more positive potential values.[61] This $E_{½}$ cumulative process is very rare[69] and no other redox reversible platform seems to be capable of making it as effectively as [**3**]$^-$. In this thesis we disclose on i) the $E_{½}$ site dependence of two opposite effect substituents, I- *vs.* Me-, all realized on boron atoms, ii) the power of the $E_{½}$ site dependence shift and iii) the application of these concepts to stabilize the $[M(C_2B_9H_{11})_2]^{2-}$ framework, [**3**]$^{2-}$, in which the M is Co^{2+} and [**4**]$^{2-}$, in which the M is Fe^{2+}.

Iodine and carbon have similar electronegativities according to the Pauling's scale, X_I= 2.66, X_C= 2.55, X_B= 2.04,[70] thus the polarization of the σ bonds for B-C and B-I shall be similar; further, both have the possibility to donate electron density to the cluster cage: iodine by π-donation and the methyl by hyperconjugation.[71] For both these

reasons, we would expect similar effects on $E_{1/2}$ by B-C and B-I substitution in $[\mathbf{3}]^-$; however for *Fc*, methyl groups produce an $E_{1/2}$ shift to more negative potentials,[72] whereas bromo groups, taken as similar to iodo, produce an $E_{1/2}$ shift towards more positive potentials, all referenced to pristine *Fc*. Therefore, there was the possibility that the opposite trend observed by alkyl or halogen substitution on *Fc* also occurred in $[\mathbf{3}]^-$, although its redox couple is $[\mathbf{3}]^{-1/-2}$ in contrast to *Fc* that is $Fc^{+/0}$. To provide evidence of this, a set of regioselective derivatives of $[\mathbf{3}]^-$ were needed.

For the voltammetric determinations, an electrochemical system, VoltaLab (Universal Electrochemical Laboratory System) interfaced with a PGZ100 potentiostat (Radiometer Analytical) and controlled by the VoltaMaster 4 software, was used. The cyclic voltammetries were performed in CH_3CN in an electrochemical cell with a standard three-electrode system (glassy carbon electrode as working electrode, $Ag/AgCl/KCl_{sat}$ as reference electrode and platinum wire as auxiliary electrode). Figure 5.1 displays a schematic drawing of the electrochemical device. The sample solutions were deoxygenated with analytical grade nitrogen at the start of each experiment to prevent oxygen interference. All experiments were performed at room temperature. Cyclic voltammogram responses were recorded at glassy carbon electrode in MeCN of 10^{-3}M sample using $[NBu_4][PF_6]$ (0.1M in CH_3CN) as supporting electrolyte. All the potential values were referred to the Fc^+/Fc couple [$E_{1/2}$ (Fc^+/Fc) = 0.64 V *vs.* Standard Hydrogen Electrode (SHE)].

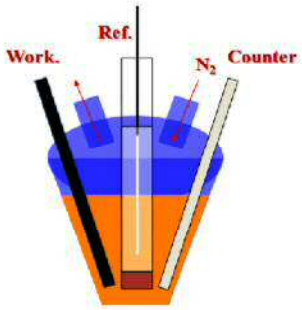

Figure 5.1. Electrochemical cell.

5.1.1.- Results of the anionic methylated cobaltabis(dicarbollide) species

Cyclic Voltammetry was run for each one of the methylated cobaltabis(dicarbollide) compounds $[Me_x\text{-}\mathbf{3}]^-$ (x= 1, 2, 4, 6, 8) that have been described in Section 2.1.1. The $E_{1/2}(Co^{3+/2+})$ potential of these species is summarized in Table 5.1.

It is observed that the substitution of B-H by B-Me induces shifts of $E_{1/2}$ to more negative potential values that are very small, between -10 / -15 mV each, thus one substitution produces -10 mV shift; two substitutions produce -20 mV; four, -40 mV; six, -90 mV; eight, -120 mV. The shift induced by each methyl unit in $[\mathbf{3}]^-$ is about ¼ of

the effected on *Fc*. Further, these changes are so small that they cannot be used to define a site effect.

Entry	Compound	Substituent' Position	$E_{1/2}$ *vs.* Fc^+/Fc	$\Delta E_{1/2}$ with respect to $[3]^-$
1	$[Me_8\text{-}3]^-$	B(8,8',9,9',10,10',12,12')	-1,92[62]	**- 0,12**
2	$[Me_6\text{-}3]^-$	B(8,8',9,9',12,12')	-1,89[62]	**- 0,09**
3	$[Me_4\text{-}3]^-$	B(9,9',12,12')	-1,84[62]	**- 0,04**
4	$[Me_2\text{-}3]^-$	B(8,8')	-1,82[62]	**- 0,02**
5	$[Me\text{-}3]^-$	B(8)	-1,81[62]	**- 0,01**
6	$[3]^-$	-	-1,80[61]	-

Table 5.1. $E_{1/2}(Co^{3+/2+})$ dependence upon the number of methyl substituents in platform $[3]^-$. $E_{1/2}$ are given in Volts.

5.1.2.- Results of the anionic iodinated cobaltabis(dicarbollide) species

Much more relevant on $E_{½}$ are the stepwise substitutions of B-H by B-I. To interpret the results, it is advisable to formally slice each half of $[3]^-$ so that four planes are generated. First plane is made of Co; second plane is made of B(4,7,8) and C(1,2); third plane is made of B(5,6,9,11,12); and fourth plane is made by B(10). The site influence on the $Co^{3+/2+}$ couple can be studied by computing the influence of each substituent on each plane on $E_{½}$. The B-I's on B(4,7,8) will tell on the effect of the substituent on the plane C_2B_3 bonded to Co. From Table 5.2 entry 2, I-B(8) in $[I\text{-}3]^-$ exerts a $\Delta E_{½}$ near +0.30V; the existence of a second I-B in the equivalent position B(8'), $[I_2\text{-}3]^-$ (Table 5.2 entry 4), induces an average $\Delta E_{½}$ per iodine atom, near +0.24V; the influence of the equivalent B(4) and B(7) sites can be obtained from $[I_4\text{-}3]^-$ in Table 5.2 entry 7 yielding an average of +0.26V, or from $[I_2\text{-}1]^-$ (Table 5.2, entry 5) with an average of +0.28V. Thus, it could be assumed that each B-I on the nearest plane to the

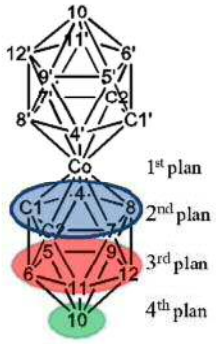

Figure 5.2. Cluster division in 4 planes.

Co, produces a $\Delta E_{1/2}$ of +0.27±0.03V. A similar process can be followed for the third plane B_5, the second nearest to Co. In this case, each B-I produces a $\Delta E_{1/2}$ of 0.15±0.03V. Finally, a B-I on the fourth plane produces a $\Delta E_{1/2}$ of +0.14V. Noticeably, these results are related to the B-I vertex distance to the Co metal center.

Entry	Compound	Substituent' Position	$E_{1/2}$ *vs.* Fc^+/Fc	$\Delta E_{1/2}$ with respect to $[3]^-$
1	$[\mathbf{3}]^-$	-	-1,80[61]	-
2	$[\mathbf{I\text{-}3}]^-$	B(8)	-1,50[62]	**+ 0,30**
3	$[\mathbf{I_2\text{-}3}]^-$	B(9,9')	-1,46[62]	**+ 0,34**
4	$[\mathbf{I_2\text{-}3}]^-$	B(8,8')	-1,32[62]	**+ 0,48**
5	$[\mathbf{I_2\text{-}3}]^-$	B(4,4')	-1,24[62]	**+ 0,56**
6	$[\mathbf{I_4\text{-}3}]^-$	B(9,9',12,12')	-1,15[61]	**+ 0,65**
7	$[\mathbf{I_4\text{-}3}]^-$	B(4,4',7,7')	-0,77[62]	**+ 1,03**
8	$[\mathbf{I_6\text{-}3}]^-$	B(8,8',9,9',12,12')	-0,82[62]	**+ 0,98**
9	$[\mathbf{I_6\text{-}3}]^-$	B(4,4',9,9',12,12')	-0,80[62]	**+ 1,00**
10	$[\mathbf{I_8\text{-}3}]^-$	B(8,8',9,9',10,10',12,12')	-0,68[61]	**+ 1,12**
11	$[\mathbf{Cl_3\text{-}3}]^-$	-	-1,53[29]	**+ 0,27**
12	$[\mathbf{Cl_6\text{-}3}]^-$	B(8,8',9,9',12,12')	-1,21[29]	**+ 0,59**
13	$[\mathbf{Cl_9\text{-}3}]^-$	-	-0,96[29]	**+ 0,84**
14	$[\mathbf{Cl_{12}\text{-}3}]^-$	-	-0,75[29]	**+ 1,05**

Table 5.2. $E_{1/2}(Co^{3+/2+})$ dependence upon the number and position of halogenated (X= I, Cl) substituents in platform $[\mathbf{3}]^-$. $E_{1/2}$ are given in Volts.

hexagon is made, as shown in Figure 5.3, and the Co is made to occupy one of the vertexes, the distance to the substituted boron in the second plane is ***d***, to the third one is 1.73***d***, and to the fourth one is 2***d***. If ***d*** is taken as 0.27, according to the influence of a B-I in the nearest plane to Co, ***d***/1.73 is 0.16 and ***d***/2 is 0.14 that nicely fits with the $\Delta E_{1/2}$ values experimentally obtained, 0.27±0.03V, 0.15±0.03V and 0.14V.

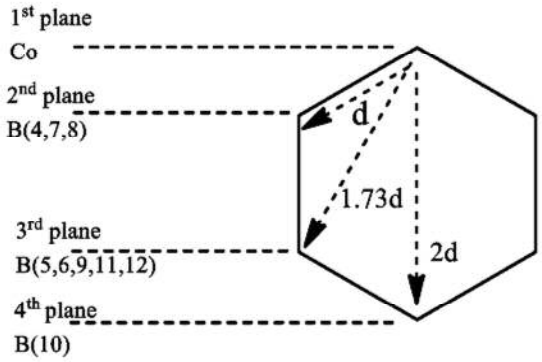

Figure 5.3. Rough approximation of the front view of the icosahedron cluster in a hexagonal representation.

The former values validate the additive rule and enlighten the importance of the site where the substitution occurs. These site dependent $\Delta E_{1/2}$ values indicate that a hypothetical [**3**]$^-$ derivative with 6 B-I in the two planes nearest to Co, would induce a global $\Delta E_{1/2}$ near +1.62V, thus converting [**3**]$^-$ with $E_{1/2}$= -1.80V into [I_6-**3**]$^-$ with $E_{1/2}$ near -0.18V. Such a synthesis is still out of the possibility of current state of the art in halogen substitution but a good approach is [I_4-**3**]$^-$ (Table 5.2, entry 7) that with 50% of the B-H replaced in [I_8-**3**]$^-$ (Table 5.2, entry 10) almost reaches the same global $\Delta E_{1/2}$ as the latter. As a proof of concept, the anion [I_6-**3**]$^-$ B(4,4',9,9',12,12') was synthesized and its expected $E_{1/2}$ should be near -0.66V. The experimental $E_{1/2}$ value is -0.80 V.

5.1.3.- Results of the anionic chlorinated cobaltabis(dicarbollide) species

Cyclic Voltammetry was run for each one of the chlorinated cobaltabis(dicarbollide) species [Cl_x-**3**]$^-$ (x= 3, 6, 9, 12) that have been described in Section 2.1.2.b. The $E_{1/2}(Co^{3+/2+})$ potential of these compounds is summarized in Table 5.2. Table 5.2 entries 8 and 12 allow to compare the different effect on the $E_{1/2}(Co^{3+/2+})$ potential of six chlorine and iodine atoms at the same framework positions, B(8,8',9,9',12,12'). The $E_{1/2}(Co^{3+/2+})$ potential of [I_6-**3**]$^-$ is -0.82 while the $E_{1/2}(Co^{3+/2+})$ potential of [Cl_6-**3**]$^-$ is -1.21. It is easily calculated that the six iodine atoms produce a $\Delta E_{1/2}$ of +0.39 V to more positive value than the six chlorine atoms bonded at the same framework position. The shift induced by each Cl atom in [**3**]$^-$ is in average about +0.1 V while each I atom induces in average a shift of +0.16 V.

5.1.4.- Results of the anionic halogenated ferrabis(dicarbollide) species

To discuss on the results, it is required to done the same as in Section 5.1.2 slicing each half of [**4**]$^-$ so that four planes are generated. First plane is made of Fe; second

plane is made of B(4,7,8) and C(1,2); third plane is made of B(5,6,9,11,12); and fourth plane is made by B(10). The site influence on the $Fe^{3+/2+}$ couple can be studied by computing the influence of each substituent on each plane on $E_{½}$. From Table 5.3 entry 3, I-B(8) in [I-**4**]$^-$ exerts a $\Delta E_{½}$ near +0.22V; the existence of a second I-B in the equivalent position B(8'), [I_2-**4**]$^-$ (Table 5.3 entry 4), induces an average $\Delta E_{½}$ per iodine atom, near +0.22V. A similar process can be followed for the third plane B_5, the second nearest to Fe. In this case [I_4-**4**]$^-$ (Table 5.3 entry 5), each B-I produces a $\Delta E_{½}$ of 0.12V. Finally, a B-I on the fourth plane produces a $\Delta E_{½}$ of +0.1V. Noticeably, these results are related to the B-I vertex distance to the Fe metal center.

From Table 5.3 entry 3 and 7, we can compare the different effect on the $E_{1/2}(Fe^{3+/2+})$ of a I and Br atoms. I-B(8) in [I-**4**]$^-$ exerts a $\Delta E_{½}$ near +0.22V while Br-B(8) exerts a $\Delta E_{½}$ near +0.14V.

Table 5.3. $E_{1/2}(Fe^{3+/2+})$ dependence upon the number and position of iodine substituents in platform [**4**]$^-$. $E_{1/2}$ are given in Volts.

Entry	Compound	Substituent' Position	$E_{1/2}$ *vs.* Fc^+/Fc	$\Delta E_{1/2}$ with respect to [**3**]$^-$ or [**4**]-
3	[I-**4**]$^-$	B(8)	-0,56[73]	**+ 0,22** **+1,24**
4	[I_2-**4**]$^-$	B(8,8')	-0,35[73]	**+ 0,43** **+ 1,45**
5	[I_4-**4**]$^-$	B(9,9',12,12')	-0,29	**+ 0,49** **+ 1,51**
6	[I_8-**4**]$^-$	B(8,8',9,9',10,10',12,12')	**+0,23**	**+ 1,01** **+ 2,03**
7	[Br-**4**]$^-$	B(8)	-0,64[31a]	**+ 0,14** **+1,16**
8	[Br_2-**4**]$^-$	B(8,8')	-0,48[31a]	**+ 0,30** **+ 1,32**
9	[Cl_6-**4**]$^-$	B(8,8',9,9',12,12')	0	**+ 0,78** **+ 1,80**
10	[Cl_8-**4**]$^-$	B(4, 4',8,8',9,9', 12,12')	**+0,22**	**+ 1,00** **+ 2,02**

Figure 5.4 clearly summarizes the tuning on the $E_{1/2}(M^{3+/2+})$, being M= Co, Fe, that can be achieved by the substitution of H atoms at the B-H vertices of the framework $[M(C_2B_9H_{11})_2]^-$ by halogenated atoms (I and Cl).

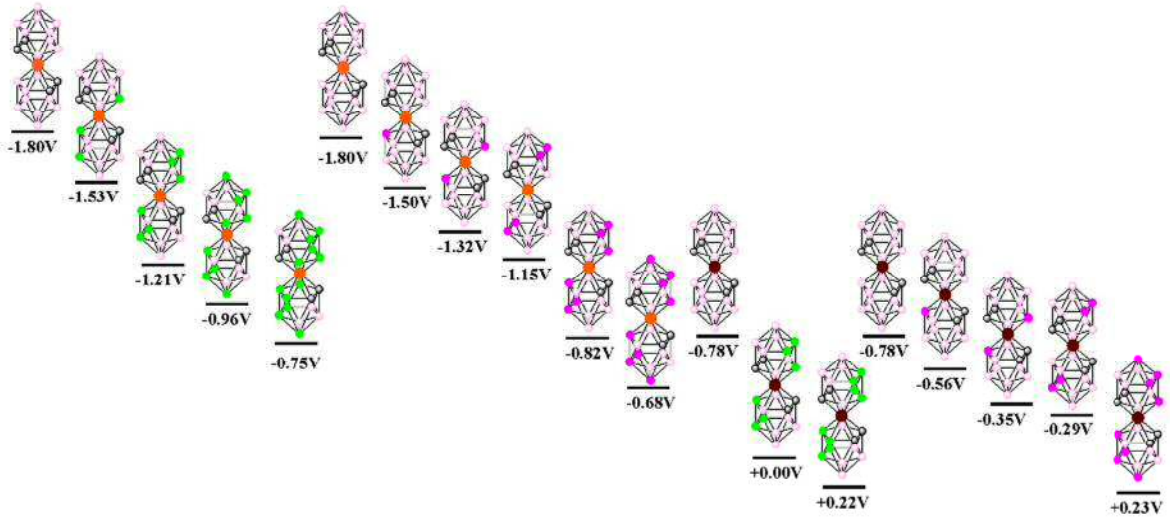

Figure 5.4. schematically display how the introduction of different substitutents to the parents $[\mathbf{3}]^-$ and $[\mathbf{4}]^-$ allow to tune the $E_{1/2}(M^{3+/2+})$, being M= Co, Fe.

This possible extended $E_{1/2}(M^{3+/2+})$ modification with a sole framework seems to be unique,[74] and its applications can be very wide in molecular electronics,[67] as electrolytes in DSSC[75] or any case where electron transfer is paramount,[51, 76] in particular when only one variable, the redox potential, is sought to be altered, as their structures can broadly be considered constant upon the addition of extra substituents. As an example, the dimensions of $[Co(C_2B_9H_{10}I)(C_2B_9H_{11})]^-$ (length (0.985 nm); width (0.656 nm))[77] do not differ much from $[Co(C_2B_9H_{10}I)_2]^-$ (length (1.018 nm); width (0.749 nm))[78] or $[Co(C_2B_9H_7I_4)_2]^-$ (length (1.235 nm); width (0.752 nm))[61], and their solubility properties differ minimally.

*5.1.5 -Electrolysis of [MV][Cl$_6$-**4**]$_2$*

As was mention before, redox couples with a sequential set of potentials are desirable for many technical applications they may have, ranging from solar cells to multi-detection electrochemical sensors.

We have studied the electrochromic behavior of the synthesized compound $[MV][Cl_6\text{-}\mathbf{4}]_2$ through electrolysis experiments. Methyl viologen (1,1′-dimethyl-4,4′-bipyridinium, MV^{2+}) has been chosen because is a well-know electrochromic material :dox processes of methyl viologen: i) the addition of one electron forms the radical cation that is intensely coloured and ii) the addition of a second electron forms a diradical neutral species that for a short time reaction, like for cyclic voltammetry conditions, is reversible.[80]

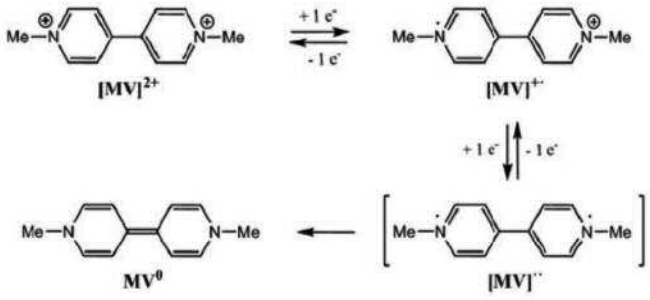

Scheme 5.1. The redox processes of $[MV]^{2+}$.

Its choise was also related to the $E_{1/2}$ of its two redox transition $E_{1/2}([MV]^{2+/+\bullet})$ = -0.82 V and $E_{1/2}([MV]^{+\bullet/0})$ = -1.23 V because these are situated in-between the $E_{1/2}$ of platform $[\mathbf{4}]^-$ $E_{1/2}([\mathbf{4}]^-$ = -0.78 V vs $Fc^{+/0}$)

The experimental setup is form by 2 compartments separated by a glass cylinder with a porous glass frit. One contains the working electrode (Pt wire), the reference electrode (Ag/AgCl/TBACl (0.1M in CH_3CN)) and the sample dissolved in the inert electrolyte (pure acetonitrile with $TBAPF_6$ 0.1 M). The second compartment had the same inert electrolyte and an auxiliary electrode (Pt wire). The separation of these solutions is required to prevent that the compound generated during the course of the electrolysis at the counter electrode react with the species that are formed at the working electrode. The MV^{2+} salt of $[Cl_6\text{-}\mathbf{4}]^-$ has been obtained as a green precipitate by mixing the water soluble $Na[Cl_6\text{-}\mathbf{4}]^-$ and a saturated solution of methyl viologen chloride, $[MV]Cl_2$. The suspension was filtrated under vacuum and washed 3 times with distilled water and then dried. The precipitation process is quantitative.

Figure. 5.5 shows the results obtained after the sequential electrolysis of $[MV][Cl_6\text{-}\mathbf{4}]_2$. In blue, we can observe the initial cyclic voltammetry of the sample that contains 2 picks from $[MV]^{2+}$ and one from the chlorinated ferrabis(dicarbollide) derivative. If we perform the sequential electrolysis at -500, -1200 and -1800 mV, we observe an intense color change (see Figure 5.5). The initial color is green, and becomes pink after electrolysis at -0.5 V. This color change is due to the $Fe^{III/II}$ process from the metallacarborane, which is fully reversible. Further reduction to -1.2 V alters the color to navy blue, which corresponds to the $[MV]^{2+/+\bullet}$ process. If a final controlled reduction is done at -1.8 V, the color of the compound is modified to orange. At the end, we have done a new cyclic voltammetry (orange dotted line) and we observe only the reversibility of the metallacarborane. MV° is no longer possible to oxidize.

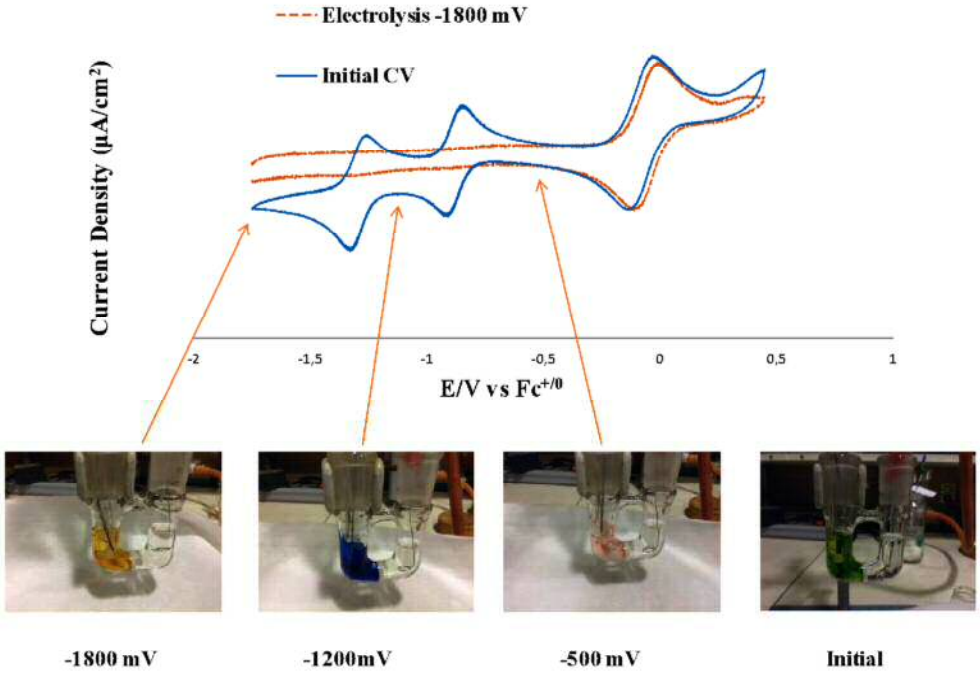

Figure 5.5. Sequential electrolysis of $[MV][Cl_6\text{-}4]_2$. Initial (blue solid line) and final (orange dotted line) CVs (after electrolysis at -1.8 V). Obtained colors after each electrolysis: orange, navy blue, pink and green.

6.1.- Ring-opening reactions of 1,4-dioxane derivative of metallabis(dicarbollide) with biomolecules

The cobaltabis(dicarbollide) anion, [**3**]$^-$, is among the boron moieties proposed for use in medicinal chemistry relatively recently.[81,82] The proton, sodium or potassium salts of this metallacarborane cluster demonstrate good solubility in water; however, the anion itself is rather lipophilic and that could have some advantages in medical applications. The problem related to the synthesis of monosubstituted functional derivatives of cobaltabis(dicarbollide) was solved when nucleophilic opening of 1,4-dioxane oxonium derivative was reported.[83] The functionalization of the [3,3'-$M(C_2B_9H_{11})_2]^-$ boron vertexes is based on the synthesis of the zwitterionic, [8-{$O(CH_2CH_2)_2O$}-3,3'-$M(1,2\text{-}C_2B_9H_{10})(1',2'\text{-}C_2B_9H_{11})$], (M = Co, **5**; Fe, **6**) derivatives.[30e,32] The cobalt-based zwitterionic compound has been proven to be susceptible to nucleophilic attack on the positively charged oxygen atom, e.g. by pyrrolyl,[30b] imide, cyanide or amines,[84] phenolate, dialkyl or diarylphosphite,[85] alcoxides,[86] and nucleosides[87] resulting once again in one anionic species formed by the cleavage of the dioxane ring (Scheme 6.1). Recent publications[88] cover the synthesis of different oxonium derivatives of polyhedral boron hydrides.

In this part of the thesis, we were concerned with the use of biomolecules as vectors for the transport of boron-enriched compounds to the specific site (cancerous cells). The following step, in the next future, would be the irradiation with slow neutrons-BNCT (as described at the Introduction), that may lead to the death of the tumour cells.

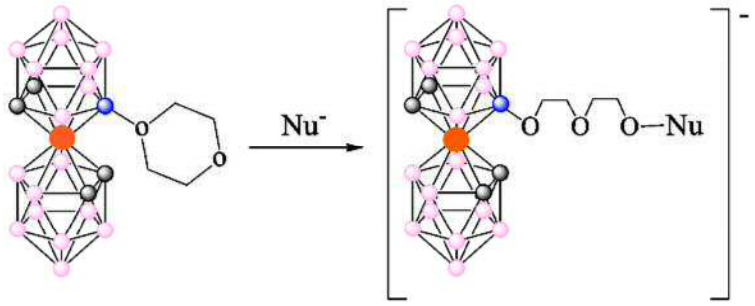

Scheme 6.1. Dioxane ring-opening reaction by a nucleofile.

6.1.1.- Syntheses of 1,4-dioxane derivative of metallaltabis(dicarbollide) clusters with biomolecules

This cyclic oxonium derivative of cobaltabis(dicarbollide) has received increased interest in these last years due to its ability to be easily attached to various substrates, including bio- and macromolecules, *via* a nucleophilic attack on the positively charged oxygen atom.[88]

In this chapter, the ring of the 1,4-dioxanate derivative of metallabis(dicarbollide), compound **5** and **6**, is cleaved by employing biomolecules such vitamins: nicotinic acid (the B_3 vitamin); fatty acid (palmitic acid) and sugars, among others.

The synthesis of such compounds is illustrated in Scheme 6.2. The first step in this dioxane ring-opening reaction was the activation of the carboxyl group of the nicotinic and palmitic acid with potassium carbonate in anhydrous acetone. Once the deprotonation process was completed (1h under reflux), metallabis(dicarbollide) dioxanate (M=Co, Fe), was added in solid state and the reaction mixture was left stirring at room temperature, overnight (Scheme 6.2). The resulting mixture was extracted with diethyl ether and for some of the compounds was necessary a purification process by preparative layer chromatography, using a mixture of CH_2Cl_2:CH_3CN (60:40).

The ring-opening reaction with the sugar have been done in dry toluene using NaH as base for removing the acidic hydrogen of the OH group. After 1 h stirring at room temperature, metallaltabis(dicarbollide) dioxanate was added as a solid. The mixture was under reflux for 3 h at 70ºC. After the extraction process, the final compound was precipitated with a saturated solution of $[NMe_4]Cl$ (Scheme 6.2).

The compounds synthesized have the general formula [3,3'-M(8-$(OCH_2CH_2)_2$R-1,2-$C_2B_9H_{10}$)(1',2'-$C_2B_9H_{11}$)]$^-$:M=Co(III) and R= COO-C_6H_5, [**7**]$^-$; R= COO-C_5H_4N, [**8**]$^-$; R= COO-$(CH_2)_{14}CH_3$, [**9**]$^-$; R= COO-sugar, [**10**]$^-$; M=Fe(III) and R= COO-C_6H_5, [**11**]$^-$; R= COO-C_5H_4N, [**12**]$^-$; R= COO-sugar, [**13**]$^-$.

Compounds [**7**]$^-$-[**10**]$^-$ were obtained with good yields (71-88%), while compounds [**11**]-, [**12**]$^-$ and [**13**]$^-$ in a 68-80% yield.

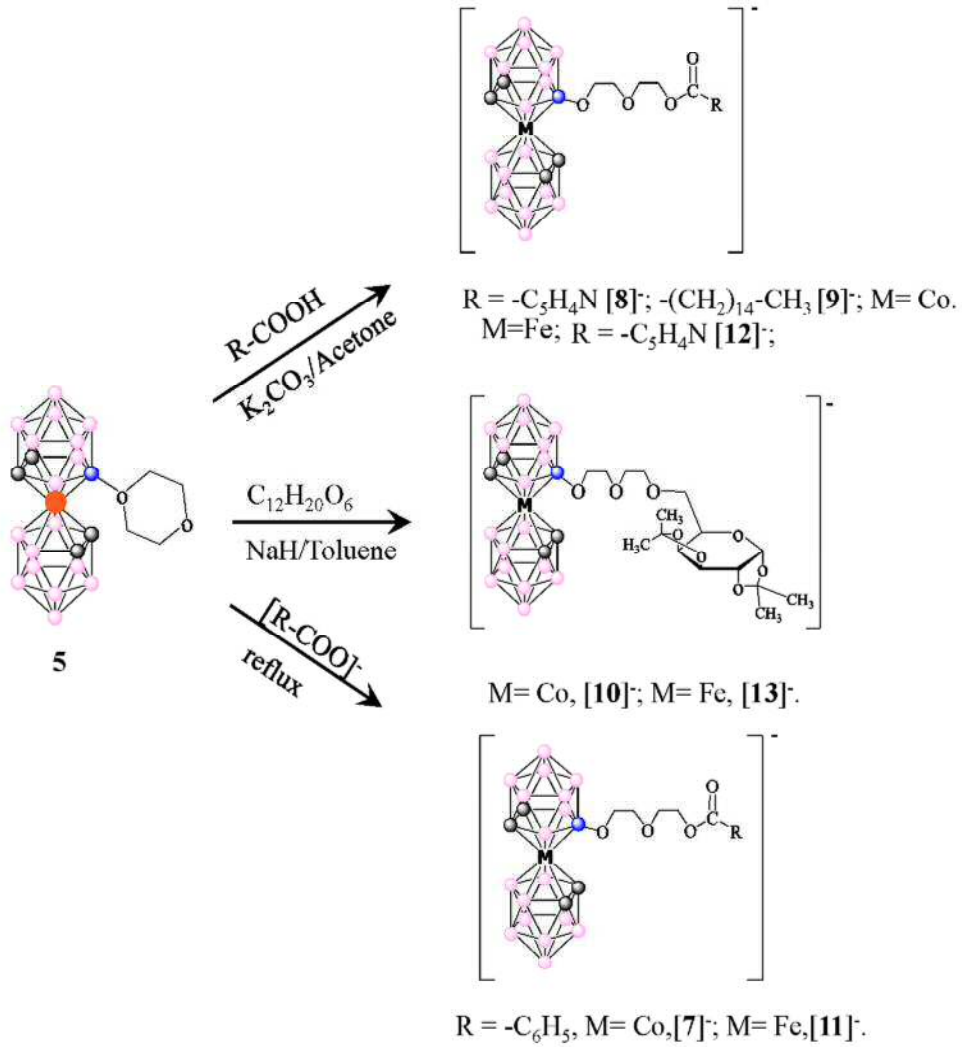

Scheme 6.2. Synthesis of novel monoanions containing biomolecules.

The final compounds were characterized using IR, MALDI-TOF-MS and ^{1}H-/$^{1}H\{^{11}B\}$-, ^{11}B-/$^{11}B\{^{1}H\}$- and $^{13}C\{^{1}H\}$-NMR spectroscopic techniques, confirming the synthesis of the desired species, with very good yields (71-88%).

Table 6.1 depictes the IR spectra of compounds [**7**]$^{-}$-[**13**]$^{-}$.

Metal	Compound	υ (C_c-H)	υ (C-H)$_{alkyl}$	υ (B-H)	υ (C=O)	υ (C-O-C)
Co	$[NMe_4][7]$[45]	3033	2959, 2918, 2866	2602, 2584, 2543	1708	1178, 1116
	K[**8**]	3003	2955, 2924, 2855	2560, 2542	1708	1172, 1092
	K[**9**]	3040	2924, 2853	2563, 2546	1720	1116, 1096
	$[NMe_4]$[**10**]	3045	2986, 2914, 2854	2538	-	1169, 1094, 1069
Fe	$[NMe_4]$[**11**]	3038	2920, 2861	2524	1708	1167, 1093
	K[**12**]	3003	2959, 2922, 2869	2560, 2546	1714	1132, 1112, 1092
	$[NMe_4]$[**13**]	3038	2985, 2923, 2864	2533	-	1166, 1068

Table 6.1. IR spectroscopy for compounds [**7**]$^-$-[**13**]$^-$.

MALDI-TOF-MS is a method of mass spectrometry in which an ion's mass-to-charge ratio is determined *via* a time measurement. This ionization technique by laser desorption, is one of the most efficient method for the characterization of the synthesized anionic clusters in solid state. As shown in Figure 6.1, the experimental molecular peak at 533.37 m/z with the isotopic distribution of one m/z units corresponds to the anion [**8**]$^-$.

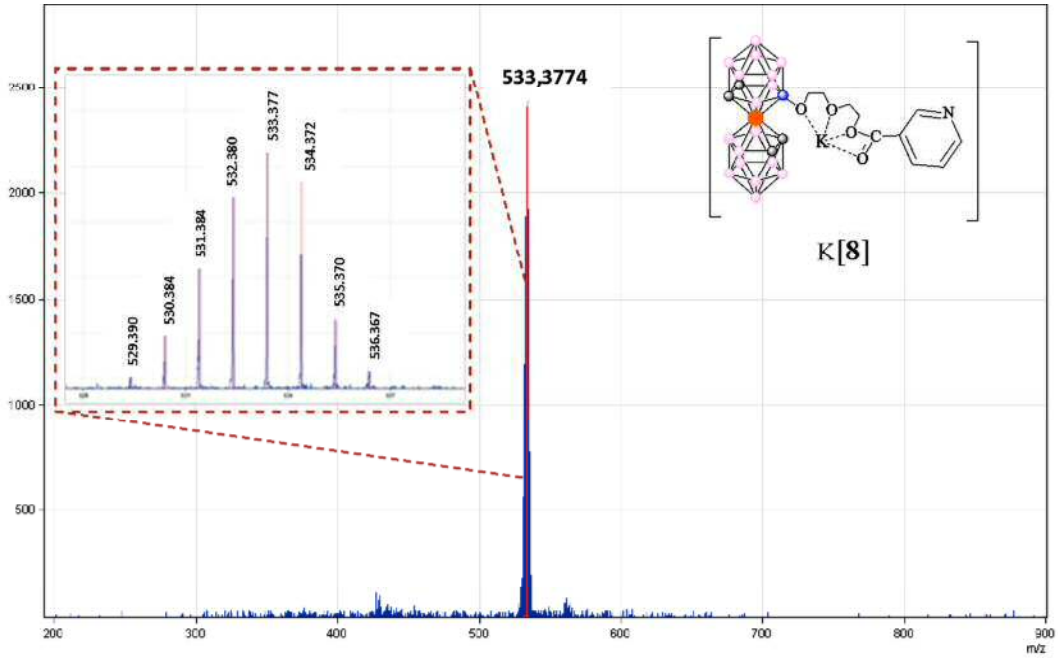

Figure 6.1. MALDI-TOF-MS spectrum of the monoanionic compound K[**8**].

Measurements of ^{1}H-NMR spectra not only complement knowledge of the individual B-H vertexes, but also provide information on the presence of C_c-H vertexes and on the existence of proton-bearing substituents as well as the presence of OCH_2 in the molecules described in this chapter. The ^{1}H-NMR spectrum of compound **[8]**$^-$ is presented in Figure 6.2 below. The ring opening reaction took place since we find the characteristic aromatic signals for the NC_5H_4 group, as the CH_2 groups corresponding to the PEG chain of the species and the C_c-H peaks. By overlapping the coupled ^{1}H-NMR (black) and decoupled ^{1}H{^{11}B}-NMR (red) spectra, one can clearly see the signals belonging to B-H bonds within the molecule, as presented in Figure 6.2 top. The fact that the peaks corresponding to the hydrogen atoms bounded to the borons are wide, is due to the coupling to boron itself, since its two isotopes have different spins and abundance (^{11}B, 80% abundance and S= 3/2; ^{10}B, 20% abundance and S= 3).

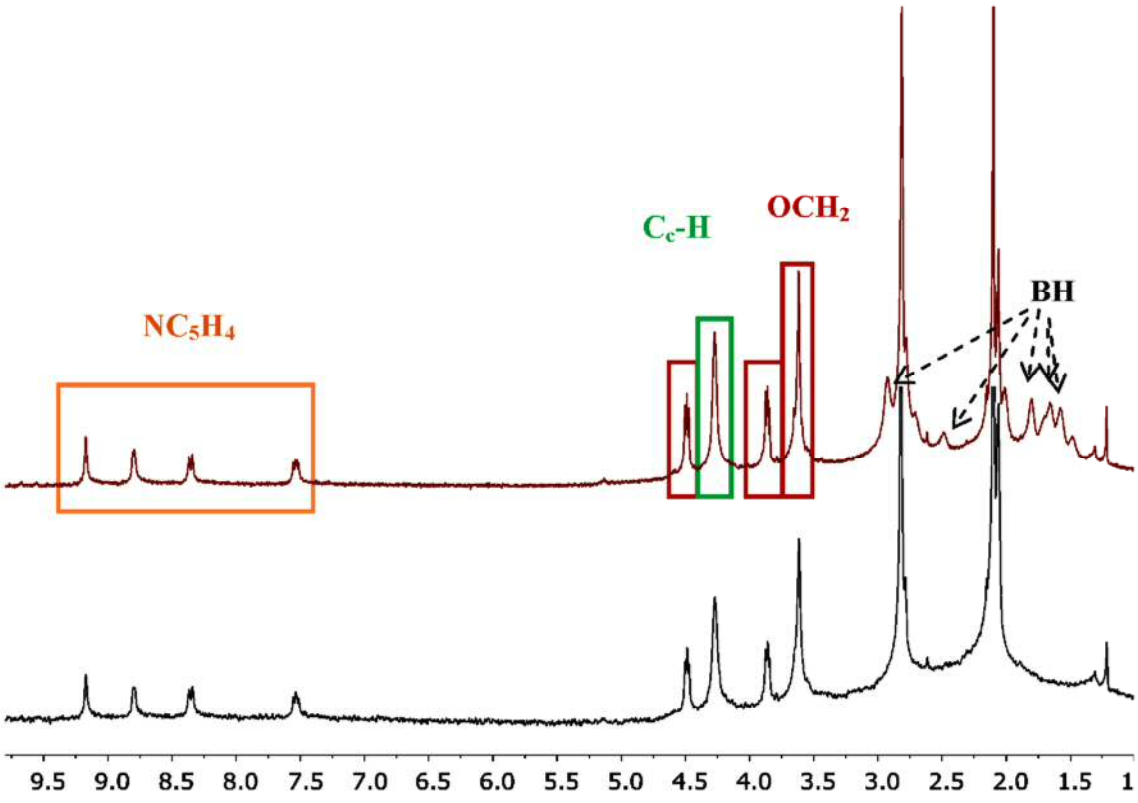

Figure 6.2. ^{1}H- and ^{1}H{^{11}B}-NMR spectra of the monoanionic compound **[8]**$^-$.

From the ^{13}C{^{1}H}-NMR spectra of compound **[8]**$^-$, represented in Figure 6.3 one can clearly see the presence of the COO^- group and the aromatic pyridyl fragment as well as the three resonances corresponding to the OCH_2 groups within the polyglycolic chain and the ones of C_c-H.

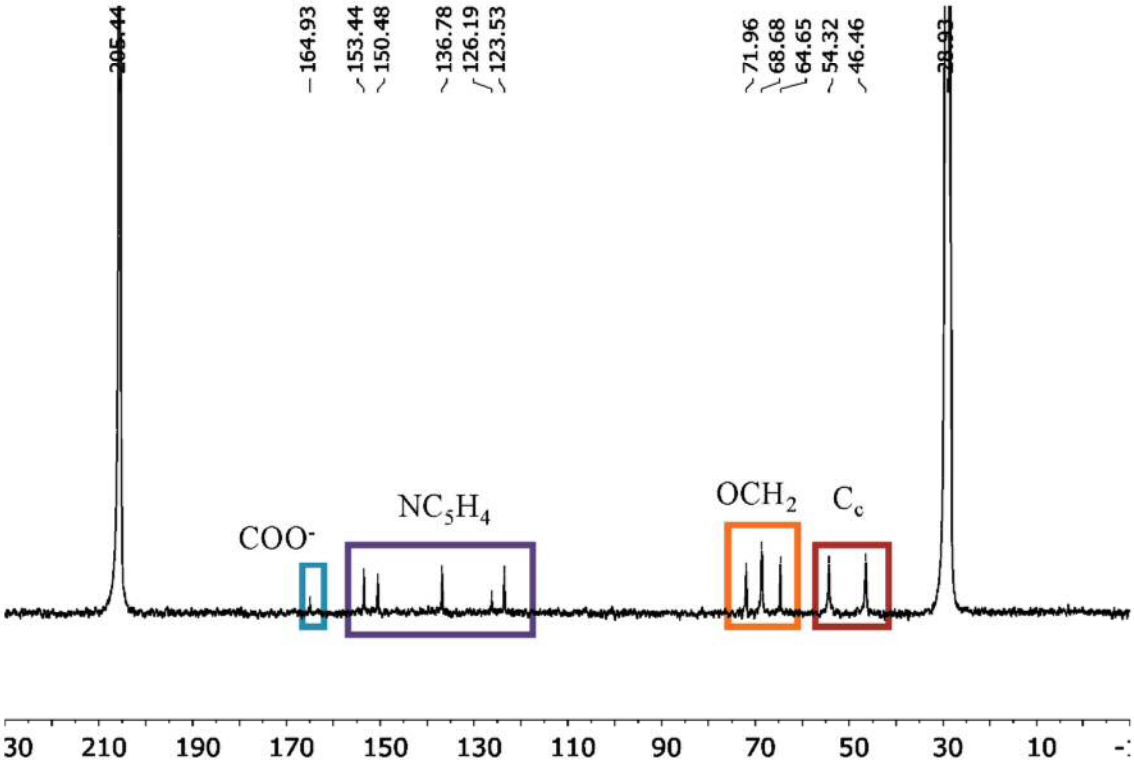

Figure 6.3. $^{13}C\{^{1}H\}$-NMR spectrum of the monoanionic compound **[8]**$^{-}$.

Regarding the $^{11}B\{^{1}H\}$-NMR spectra (Figure 6.4), the fact that the resulting

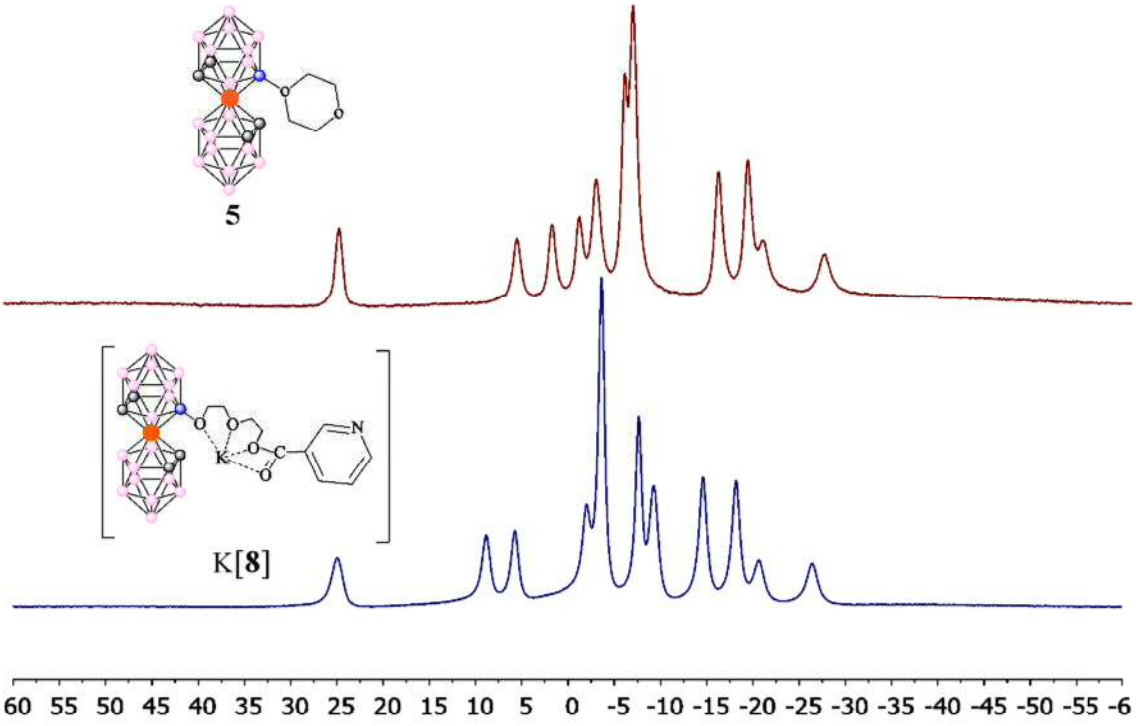

Figure 6.4. $^{11}B\{^{1}H\}$-NMR spectra of the starting zwitterion **5** (in red) and the monoanionic compound **[8]**$^{-}$ (in blue).

compounds are very similar since the substituents have no significant influence in the cluster, is translated in an unique change that is the passage from the reagent to the product; in the first case we have a boron atom, the B(8), bounded to an oxonium atom and in the final compound this boron atom is bounded to an oxygen of a PEG chain, due to ring cleavage. This difference is corresponding to a slight shift in the position of the boron atoms bounded to B(8).

The resonance at 24.3 is not split into a doublet in the ^{11}B-NMR spectrum of compound [**8**]$^-$ as shown in Figure 6.5, indicating that this resonance corresponds to the B(8)-O vertex. The observed ^{11}B-NMR pattern of compound [**8**]$^-$, 1:1:1:1:2:2:4:2:2:1:1, reflects the C_s symmetry of these monosubstituted molecules (12 different signals). The

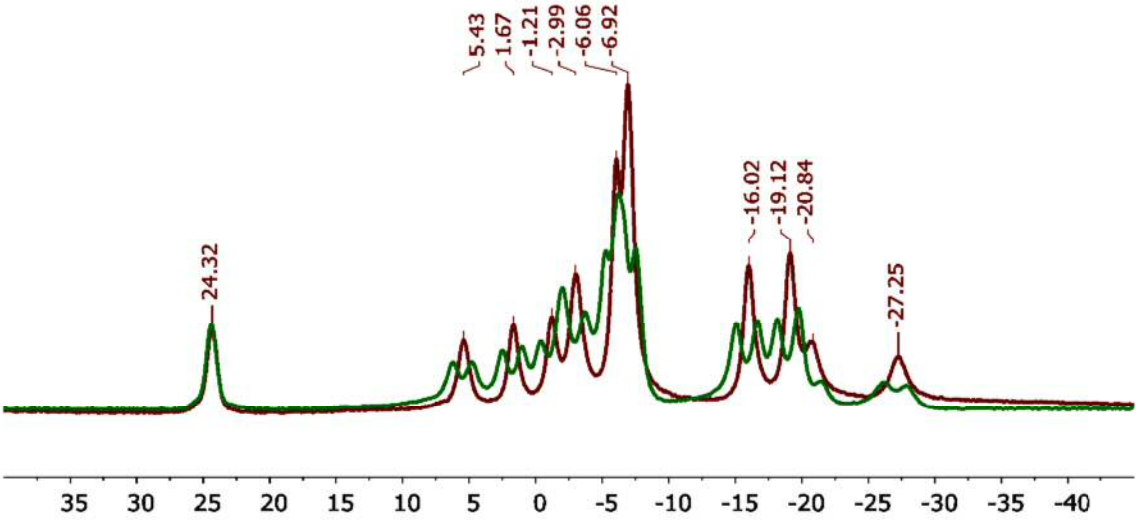

Figure 6.5. ^{11}B{^{1}H}- (red) and ^{11}B-NMR (green) spectra of [**8**]$^-$.

boron resonance with relative intensity 4 is due to coincidental overlap of two resonances with a 2:2 relative intensities. As shown in the blue spectrum of Figure 6.6, the ^{11}B{^{1}H}-NMR of [**3**]$^-$ displays five resonances in the range +6.5 to –22.7 ppm with a 2:2:8:4:2 pattern (the same as 1:1:4:2:1) in agreement with an averaged C_{2v} symmetry. The ^{11}B-NMR chemical shifts assignment of [**3**]$^-$ were determined by 2D ^{11}B{^{1}H}-^{11}B{^{1}H} COSY spectroscopy and correspond to B(8,8'), B(10,10'), B(4,4',7,7',9,9',12,12'), B(5,5',11,11'), B(6,6') from low to high field.[89] Incorporation of one substituent at position B(8) lowers the symmetry to C_s maintaining only one symmetry plane and making the two dicarbollide moieties no longer equivalent. We have reported4[b,45] that the ^{11}B-NMR spectrum of monosubstituted derivatives of [**3**]$^-$ is

the result of the plain addition of the two individual halves, as described in the section 3.1.2.

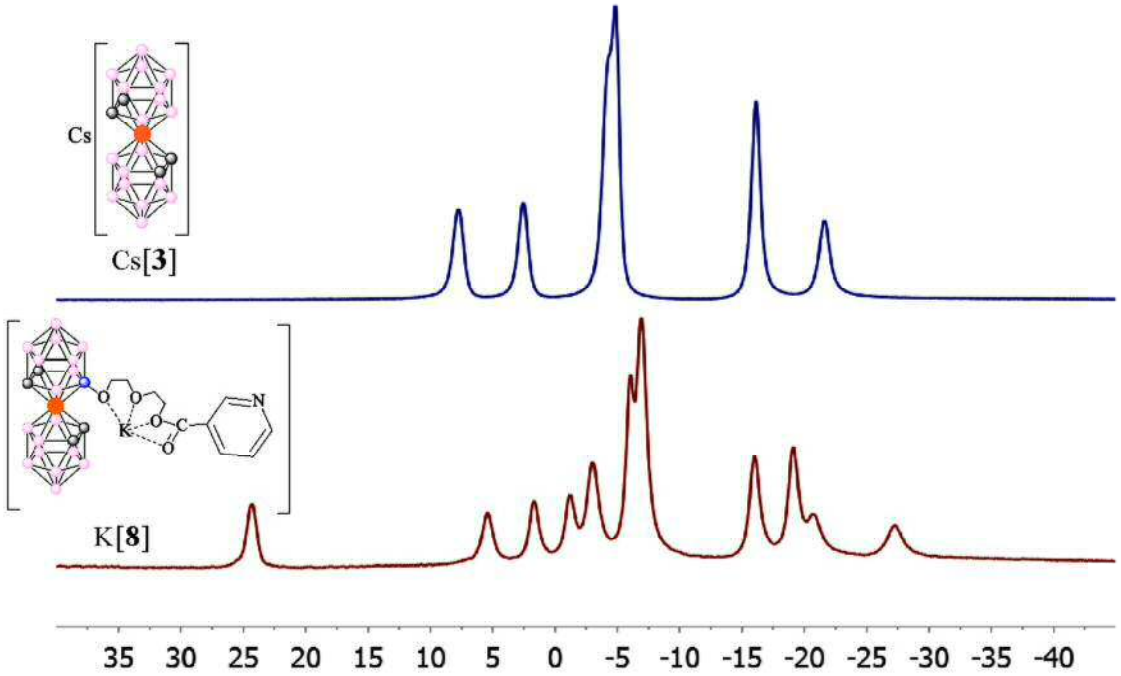

Figure 6.6. $^{11}B\{^1H\}$-NMR spectra of Cs[**3**] (in blue) and the monosubstituted K[**8**] (R= COO-C_5H_4N) (in red).

Consequently, the $^{11}B\{^1H\}$-NMR of K[**8**] is the addition of the $^{11}B\{^1H\}$-NMR of the parent [**3**]$^-$ plus the spectrum of the unknown [3,3'-Co((8,8'-$(OCH_2CH_2)_2R)_2$-1,2-$C_2B_9H_{10})_2]^-$. The spectrum of [**3**]$^-$ displays resonances at 6.5(1), 1.4(1), -6.0(4), -17.2(2) and -22.7(1) ppm and the spectrum of [3,3'-Co(8-$(OCH_2CH_2)_2$R-1,2-$C_2B_9H_{10})$(1',2'-$C_2B_9H_{11})]^-$ (R= COO-C_5H_5N) at 24.4(1), 5.6(1), 1.8(1), -1.1(1), -2.9(2), -6.0(4), -6.8(2), -15.8(2), -18.9(2), -20.6(1) and -27.0(1) ppm. If resonances attributable to the unsubstituted ligand, showing only minor shifts in respect to parent [**3**]$^-$ are removed, the resonances of the unknown disubstituted [3,3'-Co(8,8'-$(OCH_2CH_2)_2R)_2$-1,2-$C_2B_9H_{10})]^-$ ligand could be assigned at 24.4(1), -1.1(1), -2.9(2), -6.8(2), -18.9(2) and -27.0(1) ppm. The 1:1:2:2:2:1 pattern is consistent with a C_s fragment symmetry, and the high chemical shift value at 24.4 strongly supports assignment to B(8)-O-.

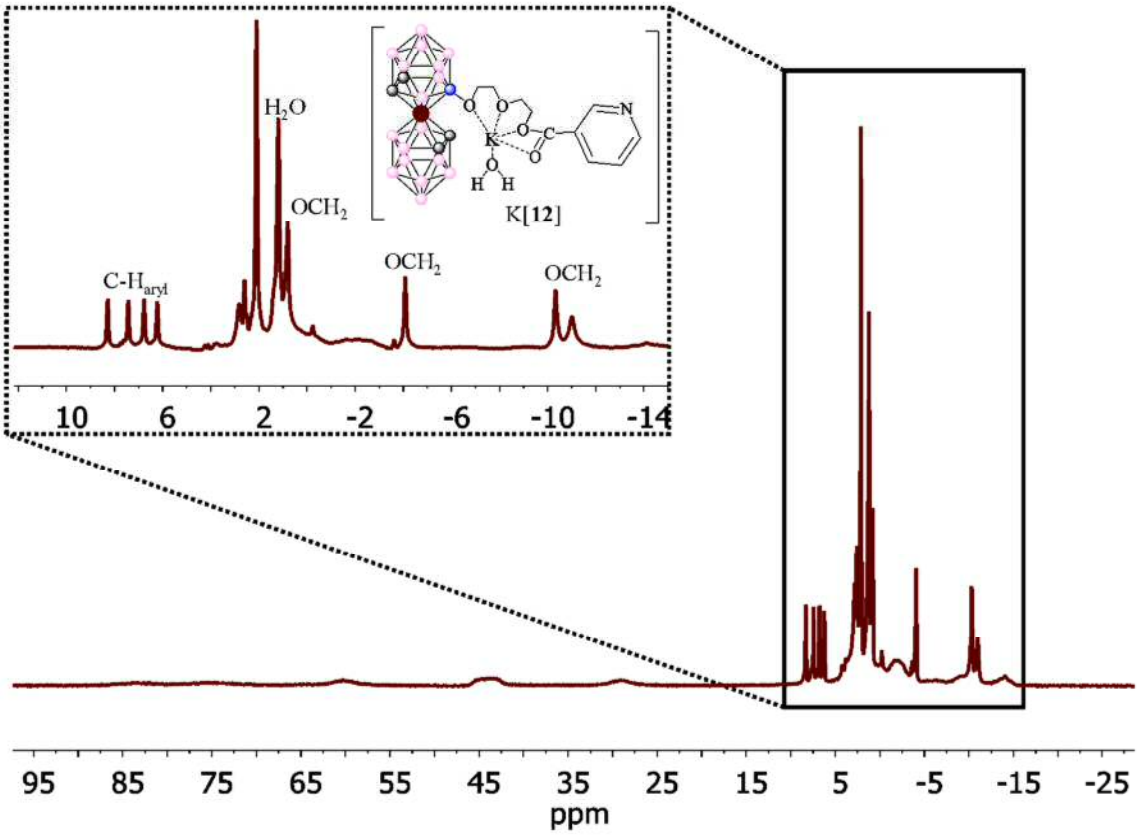

Figure 6.7. ^{1}H-NMR of the paramagnetic [**12**]$^{-}$.

The ^{1}H-NMR spectra of the anionic ferrabis(dicarbollide) derivatives, [**11**]$^{-}$-[**13**]$^{-}$**,** exhibit considerable paramagnetic shifting of all signals of the branch with respect with the corresponding diamagnetic ones, [**7**]-[**10**]$^{-}$, most pronounced being the broad signal of C_c-H protons found +42.8 and +44.4 ppm; +43.2 and 44.8; +43.1 and +44.7 for [**11**]$^{-}$, [**12**]$^{-}$ and [**13**]$^{-}$, respectively. As an example, Figure 6.7 displays the ^{1}H-NMR of the paramagnetic species [**12**]$^{-}$. The influence of a paramagnetic metal ion within a molecule actually changes its NMR spectrum because it affects the chemical shifts, the ^{1}J splitting, and the relaxation rates of the nuclear signals.[90] To notice in Figure 6.7 is the influence of the proximity of the OCH_2- groups on the paramagnetic Fe(III) center: i) namely the closer to the Fe(III) center, the more shifted to higher field, and ii) there is apparently no ^{1}J(H,H) coupling between the CH_2 groups of the polyether branch.

The paramagnetic monobranched species, [**11**]$^{-}$–[**13**]$^{-}$, possesses two different carboranyl moieties, {8-$(OCH_2CH_2)_2$R-1,2-$C_2B_9H_{10}$} and {1',2'-$C_2B_9H_{11}$}, which are clearly observed in their ^{11}B NMR spectrum as the addition of the two individual halves.

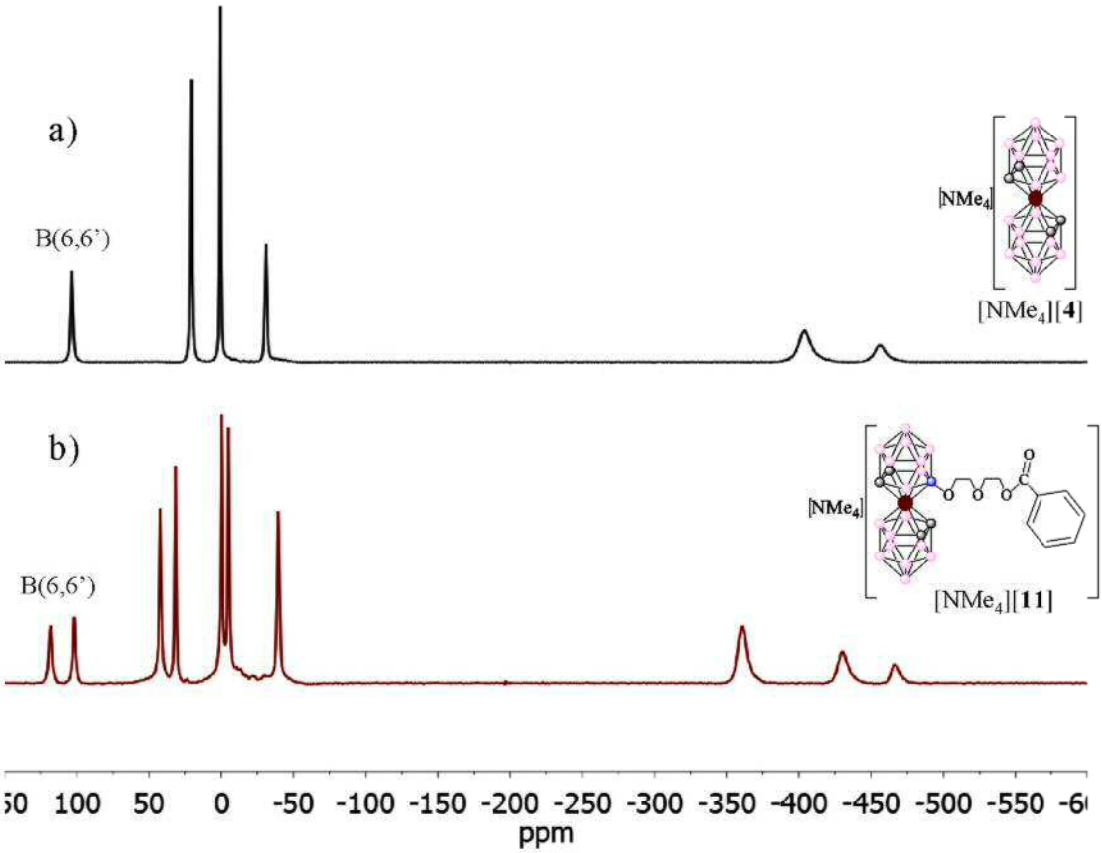

Figure 6.8. ^{11}B NMR spectra of $[NMe_4]$[**4**] and $[NMe_4]$[**11**].

When comparing Figure 6.8a and 6.8b, the asymmetry induced by the presence of the substituent at B(8) is clearly detected by the duplicity of the related peaks.

6.1.2.- Syntheses of bifunctional derivative of cobaltabis(dicarbollide) with biomolecules and iodine

Despite the large variety of cobaltabis(dicarbollide) derivatives proposed in the literature as potential Boron Neutron Capture Therapy (BNCT) drug candidates, only a few of them have been actually assayed "*in vivo*", mainly due to the lack of efficient and non-invasive methods suitable for the determination of the boron concentration in the tumour over time. Such information would facilitate preliminary screening of compounds and selection of the most promising drug candidates. In this context, nuclear imaging techniques such as Positron Emission Tomography (PET) and Single Photon Emission Computerized Tomography (SPECT) might be extremely helpful, as they can provide accurate information about the spatiotemporal distribution of a labeled

compound after administration into a living organism, with high sensitivity and non-invasively.

In the pursuit of labelling strategies for the incorporation of positron and gamma emitters in boron rich structures, we have designed the synthesis of new bi-functional (iodine and polyethylene glycol, PEG) cobaltabis(dicarbollide) derivatives. These mixed-doubly functionalized cobaltabis(dicarbollide) compounds incorporate simultaneously two markedly different reactive sites: a PEG branch and a suitable iodinated moiety for subsequent incorporation of the radioisotope.

The synthesis of the new bi-functional cobaltabis(dicarbollide) derivatives, [3,3'-M(8-$(OCH_2CH_2)_2$R-1,2-$C_2B_9H_{10}$)(8'-I-1',2'-$C_2B_9H_{10}$)]$^-$:M=Co(III) and R= COO-C_6H_5, [I-**7**]$^-$; R= COO-C_5H_4N, [I-**8**]$^-$; R= COO-$(CH_2)_{14}CH_3$, [I-**9**]$^-$; R= COO-sugar, [I-

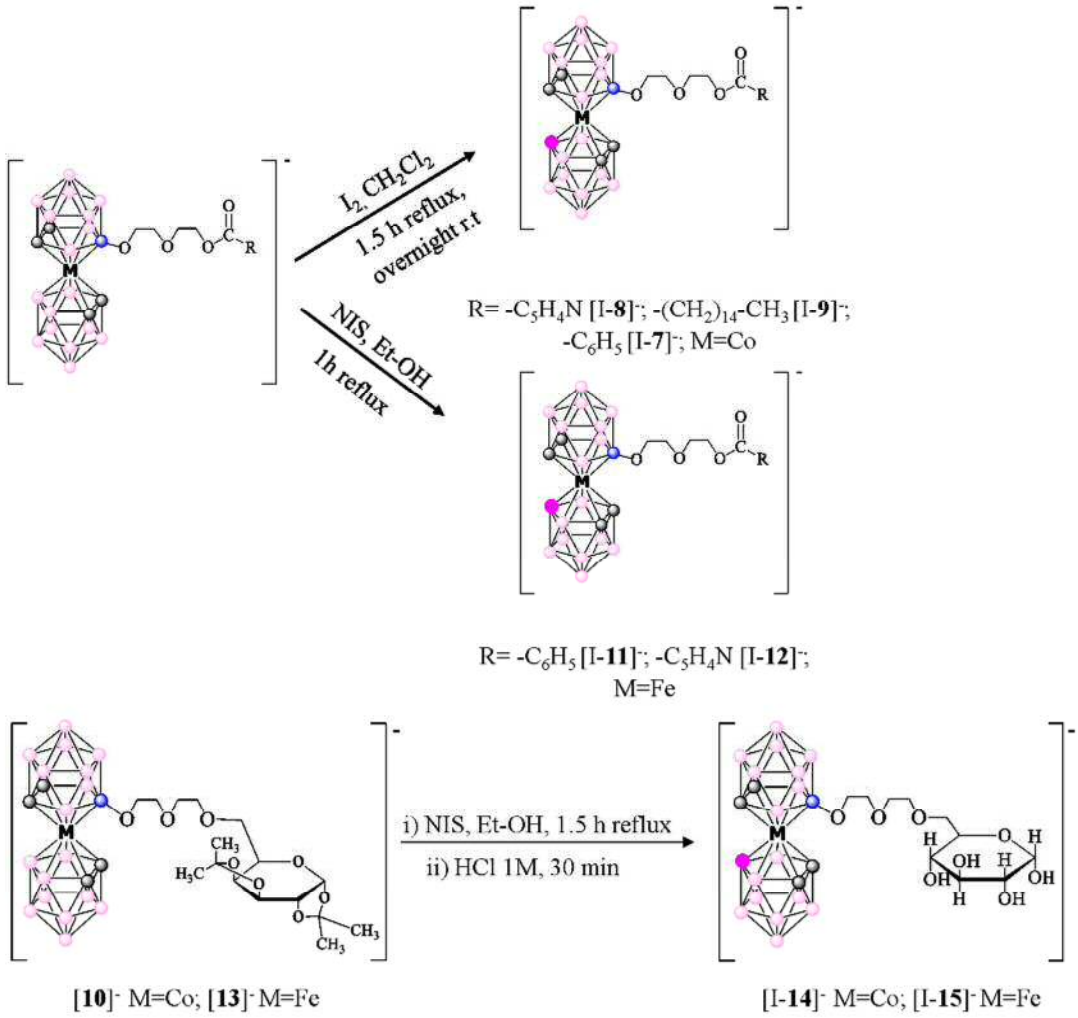

Scheme 6.3. Synthesis of mixed doubly functionalized derivative of metallabis(dicarbollide), M= Co, Fe.

14]$^-$; M=Fe(III) and R= COO-C_6H_5, [I-**11**]$^-$; R= COO-C_5H_4N, [I-**12**]$^-$; R= COO-sugar, [I-**15**]$^-$, was carried out following the Scheme 6.3.

To be emphasized that the iodination reaction conditions on compound [**10**]$^-$ produces the cluster iodination and deprotection of the sugar at once, so compound [I-**14**]$^-$ was obtained.

As one example of the compounds synthesis, to a solution of Na[3,3'-Co(8-$(OCH_2CH_2)_2$R-1,2-$C_2B_9H_{11}$)(1,2-$C_2B_9H_{11}$)] in CH_2Cl_2, iodine was added in a molar ratio 1:2. The reaction mixture was left to stand overnight at room temperature and then heated under reflux for 1.5h. The excess of iodine was quenched with aqueous Na_2SO_3 solution, the resulting mixture was evaporated, and the orange solid washed with water before being extracted with diethyl ether (3x10mL). After drying over anhydrous $MgSO_4$, the organic layer was evaporated to obtain Na salt of the bifunctional derivatives in 81-73% yield.

The final compounds were characterized using IR, MALDI-TOF-MS and ^{1}H-/^{1}H{^{11}B}-, ^{11}B-/^{11}B{^{1}H}- ,^{13}C{^{1}H}-NMR spectroscopies, confirming the synthesis of the desired species.

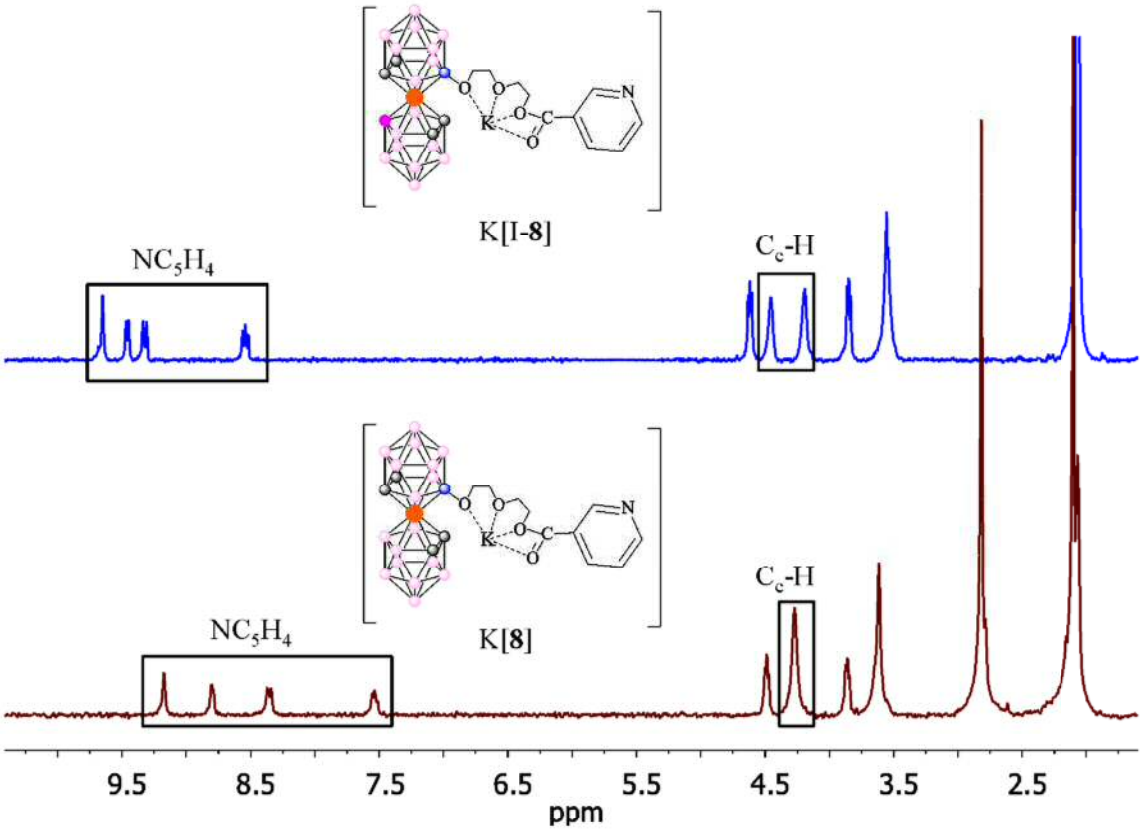

Figure 6.9. ^{1}H-NMR spectra of K[**8**] (red) and K[I-**8**] (blue).

The MALDI-TOF analysis of K[I-**8**] compound showed the desired molecular peak at 659.28 m/z corresponding to M (100%) and a fragmentation peak at 553.26 (M-I, 6%). The IR showed bands at 3040, 2947-2869, 2568-2539, 1736 and 1100-1071 cm^{-1} corresponding to C_c-H, C_{alkyl}-H, B-H, C-O-C and O-C-O, respectively.

Figure 6.9 compares the ^{1}H-NMR spectra of K[**8**] and its iodinated one K[I-**8**]. To emphasize that iodination produces: i) the hydrogen atoms of the aromatic group move down field with respect to the non-iodinated compound and, ii) the H atoms bonded to Cc split in two broad singlet at δ 4.45 and 4.19 ppm, one resonance from each moiety. The explanation could be that the monoanionic [I-**8**]$^-$ is forced to be arranged in a *transoid* conformation from the repulsion of the lone pairs of I and O atoms. This conformation produces a quite short contact between the C_c-H from one moiety and I atom of the other one producing intramolecular C_c-H···I hydrogen bonds.

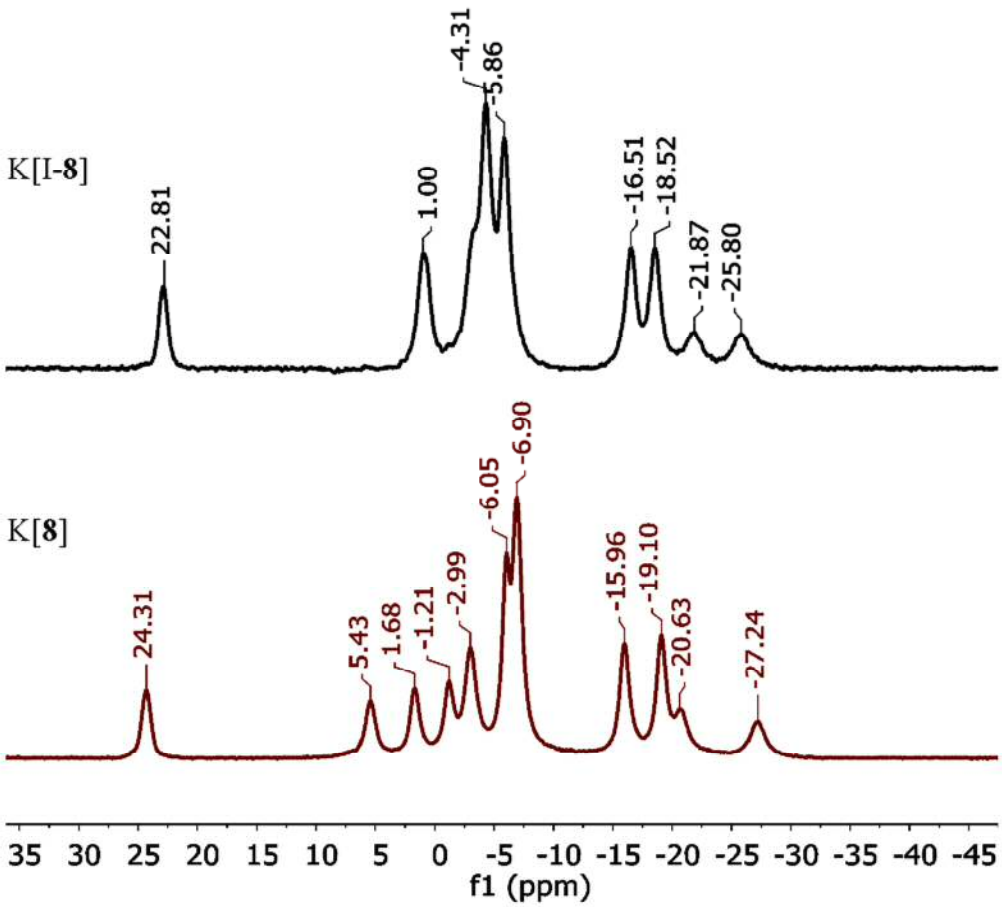

Figure 6.10. ^{11}B{^{1}H}-NMR spectra of K[**8**] (in red) and K[I-**8**] (in black).

Figure 6.10 display the comparison between the ^{11}B{^{1}H}-NMR spectra of K[**8**] and K[I-**8**] with an average chemical shift , <δ(^{11}B)> of the order of ca. -9.04 ppm and -7.41

ppm, respectively.

7.1.- Applications

7.1.1.- Medicine

After the synthesis of monobranched polyethoxylated cobaltabis(dicarbollide) derivatives described in the preview section, we developed a strategy to covalently label this compounds with either ^{125}I (gamma emitter) or ^{124}I (positron emitter) via palladium catalyzed isotopic exchange. All this studies have been done in collaboration with Dr. Jordi Llop, from Radiochemistry and Nuclear Imaging Department of biomaGUNE. As you can observe, the compound [I-**7**]$^-$ has two different reactive sites: one iodine atom that can be radiollabelled and a PEG branch ending with a biomolecule that acts as the vector. The incorporation of ^{125}I and ^{124}I enables the evaluation of their biodistribution pattern in rodents using PET and dissection/gamma counting has been studied for the first time. Radiolabelling reactions on compounds Na[I-**7**] and Na[I-**3**] were performed by adapting the previously reported palladium catalyzed iodine exchange reaction on iodinated dicarba-*closo*-dodeca borane.[82b] The Na[I-**3**] has been taken as reference just

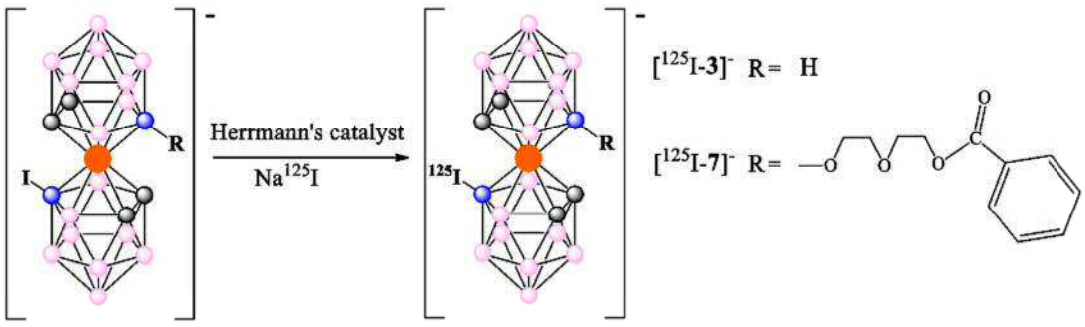

Scheme 7.1. Radioiodination reaction of mono anionic [^{125}I-**3**]$^-$ and [^{125}I-**7**]$^-$. Reaction conditions for [^{125}I-**3**]$^-$: Na[^{125}I]I, Herrmann's catalyst, toluene, 100 °C, 3 min. Reaction conditions for [^{125}I-**7**]$^-$: Na[^{125}I]I, Herrmann's catalyst, toluene, 80 °C, 8 min.

to see the influence of the second branch. Experimental conditions were first optimized using ^{125}I, which is a convenient radioisotope due to its long half-life (59.4 d) and low cost.

Radiochemical conversion values close to 85% were achieved for compound [I-**3**]$^-$ when the reaction was conducted at 100℃ for

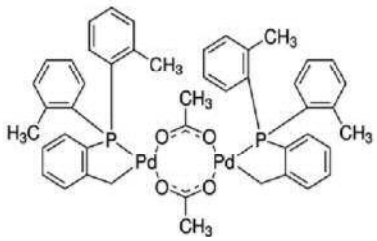

Figure 7.1. Herrmann's catalyst *trans*-Bis(acetato)bis[o-(di-o-tolylphosphino)benzyl]dipalladium(II).

3 min, as determined by high performance liquid chromatography (HPLC) using radiometric detection; longer reaction times did not improve radiochemical conversion. For compound [I-**7**]$^-$, the formation of unidentified labelled species was detected when the reaction was conducted at 100 ℃. Lower reaction temperatures (80 ℃) led to almost 80% radiochemical conversion after 8 min (Scheme 7.1). Purification by semi-preparative HPLC followed by solvent evaporation and reconstitution with C_2H_5OH–H_2O (1/9) resulted in injectable solutions of chemically and radiochemically pure compounds.

Next step was the determination of the lipophilicity of the radiolabelled compounds. Lipophilicity is a fundamental physicochemical property of a ligand and plays a pivotal role in the absorption, distribution, metabolism and elimination of drug molecules. Molecular size, mass and hydrogen bonding capacity also contribute to the overall lipophilicity of the compound.[91] Lipophilicity was calculated by the distribution coefficient (Log D)[92] and the values were 1.1± 0.1and 1.5 ±0.1 for [^{125}I-**3**]$^-$ and [^{125}I-**7**]$^-$, respectively. These results indicate that the presence of the PEG arm in [I-**7**]$^-$ results in a slight increase in the lipophilicity.

Biodistribution studies using dissection and gamma counting were performed in rodents. Three animals per compound were used. Anesthesia was induced with 3% isoflurane and maintained by 1.5 to 2 % of isoflurane in 100% O_2. For intravenous administration of the radiotracer, the tail vein was catheterized with a 24-gauge catheter and the radiotracer (25 ± 5 μCi, 100 μL) was injected. The animals were kept under anesthesia throughout the duration of the study. At pre-selected time points (10, 30 and 120 minutes after administration) animals were sacrificed by exsanguination. The animals were perfused with saline solution, the organs were harvested, weighted and the amount of radioactivity was determined using a gamma counter. Comparison with a standard calibration curve enabled the determination of accumulated radiotracer as percentage of injected dose per gram of tissue (Figure 7.2 a and b).

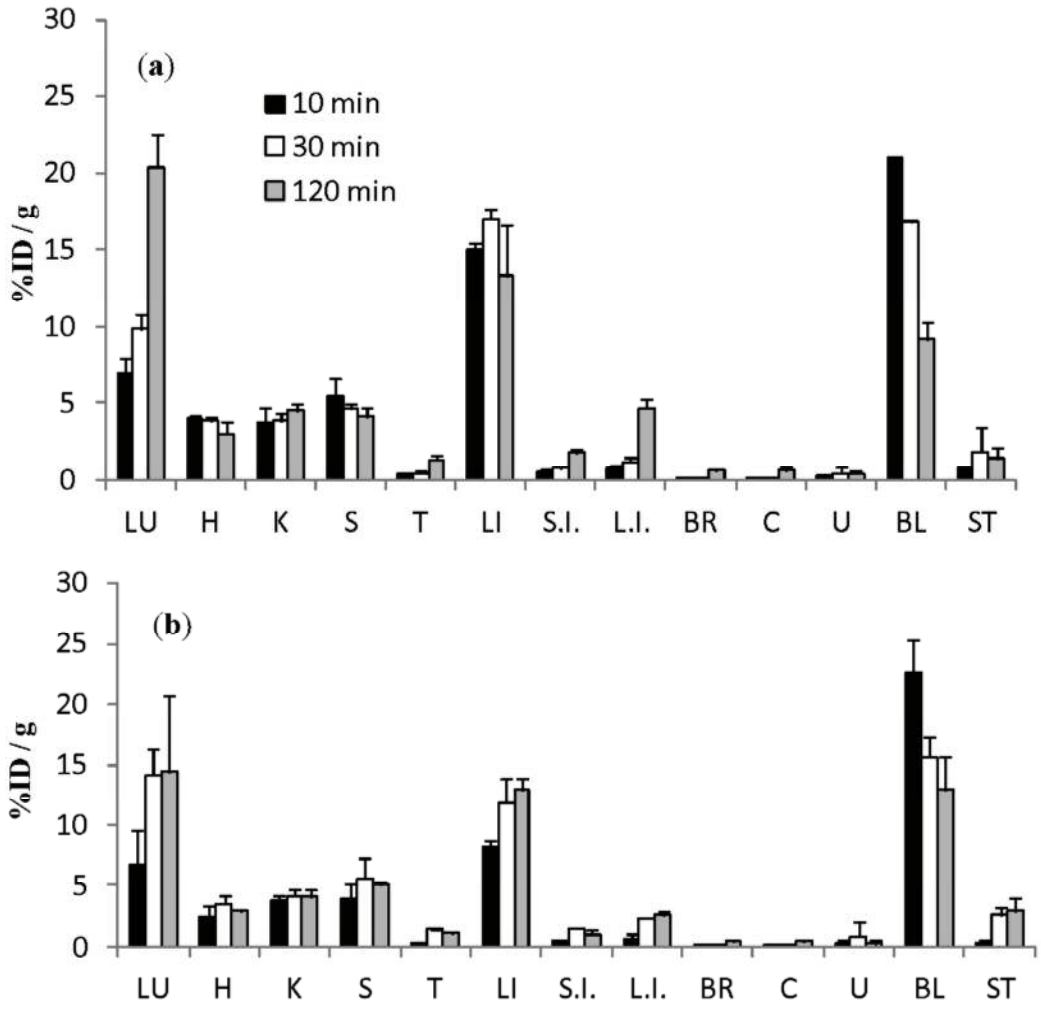

Figure 7.2. Accumulation of radioactivity in different organs for the compounds [^{125}I-**3**]$^-$ **(a)** and [^{125}I-**7**]$^-$ **(b)** using dissection and gamma counting at selected time points after administration, results are expressed as % of injected dose (%ID) per gram of tissue.

Very similar patterns were obtained for both compounds: high accumulation in the liver throughout the duration of the study, increasing uptake in the lungs and moderate blood clearance. Uptake in the kidneys and the spleen was also significant and lower accumulation was detected in other organ. Progressive accumulation in the intestine and the low concentration of radioactivity in the bladder (urine) suggest biliary excretion.

In vivo positron emission tomography (PET) biodistribution studies were performed on healthy mice using ^{124}I-labelled compounds; the radiolabelling process was performed following the optimized experimental conditions developed for ^{125}I, with

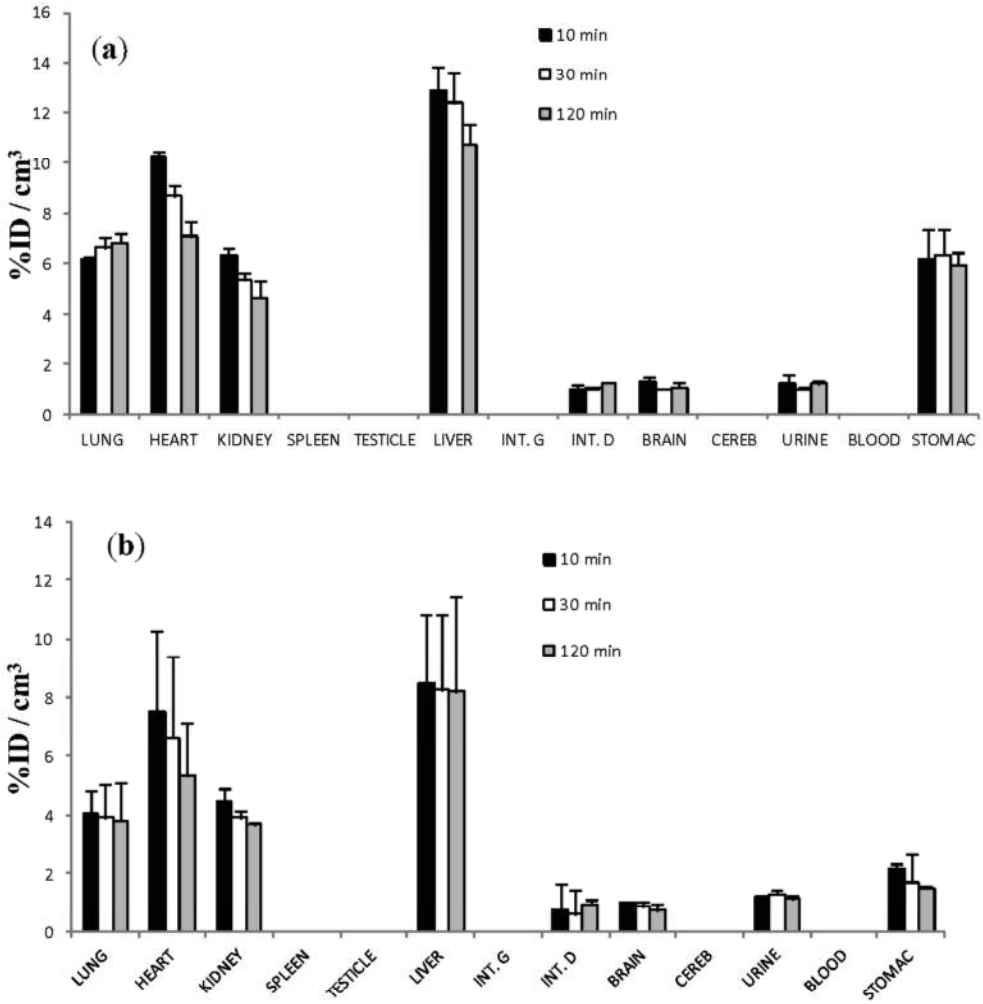

Figure 7.3. Accumulation of radioactivity in different organs for the compounds [^{124}I-**3**]$^-$ **(a)** and [^{124}I-7]$^-$ **(b)** determined by PET-CT at selected time points after administration; results are expressed as % of injected dose (%ID) per cm^3 of tissue. Mean ± standard deviation values are presented (n=3).

equivalent incorporation ratios. So, after anesthesia procedure, the radiotracer was injected concomitantly with the start of a PET dynamic acquisition. After each PET scan, Computerized Tomography (CT) acquisitions were also performed, providing anatomical information as well as the attenuation map for the later image reconstruction (Figure 7.4). Just the organs clearly visualized on the CT images (lungs, heart, kidneys,

liver, intestine, brain, bladder and stomach) were analyzed (Figure 7.3.). Results showed major accumulation in liver, heart, lung kidney and stomach.

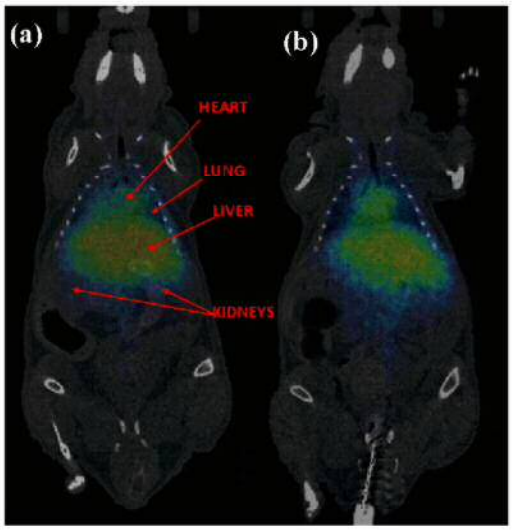

Figure 7.4. PET projections resulting from averaged images obtained after administration of [^{124}I-**3**]$^-$ **(a)** and of [^{124}I-7]$^-$ **(b)**.

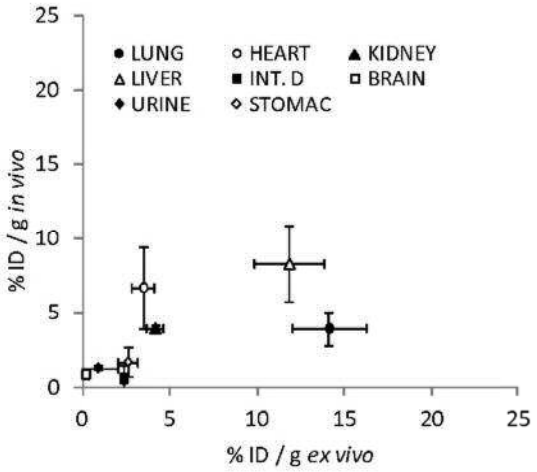

Figure 7.5. Correlation between results obtained using PET-CT (expressed as %ID/cm^3 of tissue) and dissection and gamma counting (expressed as %ID/g of tissue) for compound [^{125}I-**3**]$^-$ at 30 minutes after administration.

A good correlation between results obtained using both methodologies (*in vivo* imaging and dissection/gamma counting) was obtained (Figure 7.5) although significant differences were observed at different time points in the brain, the bladder and the lungs. As a general trend, higher accumulation values in the brain were obtained *in vivo*, probably due to the contribution of the blood to the overall quantification of the uptake in this region. In the particular case of the lungs, the differences can be attributed to the fact that the percentage of injected dose (%ID) per gram of tissue is measured *ex vivo*, whereas *in vivo*, the %ID per cm^3 is obtained. Because the density of the lungs significantly differs from 1 g cm^{-3}, the results obtained in both experiments cannot be directly compared. Differences observed in the bladder might be due to urination during image acquisition (*in vivo*) or uptake time (*ex vivo*).

Interestingly, *in vivo* studies did not show accumulation of radioactivity in the thyroid gland, suggesting the stability of both [^{124}I-**3**]$^-$ and [^{124}I-**7**]$^-$.

The general radiolabelling strategy reported here, which can be applied in the future to cobaltabis(dicarbollides) derivatives bearing a wide range of functionalities might be applicable to targeted cobaltabis(dicarbollides) able to selectively accumulate in tumours. Hence, our method may become an invaluable, widely applied tool for the

fast and accurate evaluation of new cobaltabis(dicarbollides)-based BNCT drug candidates in animal tumour models.

This study confirms the stability of the boron clusters and beside they have many properties similar to the organic ones, they are not detected (so no metabolized) by the enzyme because of their inorganic nature.

After the biodistribution studies with cobaltabis(dicarbollide) derivatives in healthy mice, we performed *in vivo* studies, in tumour model with the following compounds: K[I-**9**], H[I-**14**] and Na[I-**3**]. Radiolabelling reactions were performed by adapting the previously reported palladium catalyzed iodine exchange reaction (Scheme 7.2). For those labelled compounds not previously reported (K[I-**9**], H[I-**14**]) experimental conditions were first optimized using ^{125}I, which is a convenient radioisotope due to its low cost.

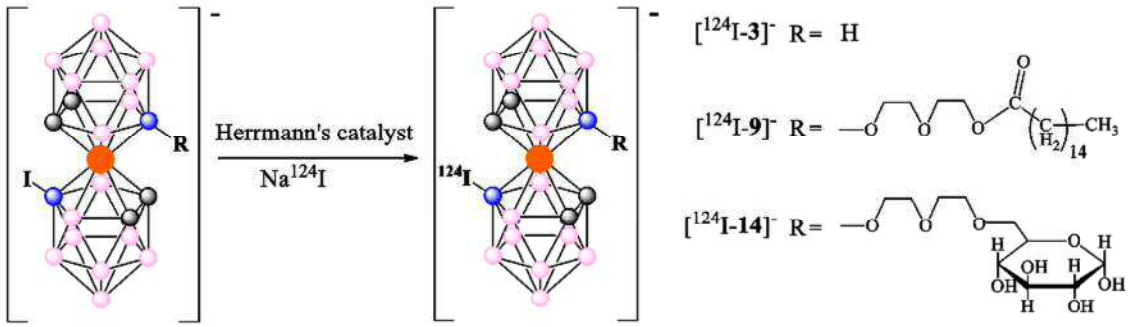

Scheme 7.2. Radioiodination reaction of [^{124}I-**3**]$^-$, [^{124}I-**9**]$^-$ and [^{124}I-**14**]$^-$. Reaction conditions for [I-**3**]$^-$: T=100°C, t=3 min; Reaction conditions for [I-**9**]$^-$: T=70°C, t=15 min; Reaction conditions for [I-**14**]$^-$: T=90°C, t=10 min.

Briefly, the appropriate precursor was reacted with 740-148 KBq (20-40 μCi) of Na[^{125}I]I (solution in 0.1M aqueous NaOH) in the presence of Herrmann's catalyst (0.1mg). Radiochemical conversion values, as determined by high performance liquid chromatography (HPLC) using radiometric detection were 48±6%, 67±4% and 32±7% for [I-**3**]$^-$, [I-**9**]$^-$ and [I-**14**]$^-$, respectively, when the reaction conditions were T=100 °C, t=3 min for [I-**3**]$^-$; T=70 °C, t=15 min for [I-**9**]$^-$ and T=90 °C, t=10 min for [I-**14**]$^-$.

Experimental conditions were then translated to ^{124}I. The procedure was exactly the same, but Na^{124}I (solution in 0.2M NaOH) was used instead of Na^{125}I. After the labelling reaction, purification was achieved by semi-preparative HPLC followed by reconstitution with solid phase extraction, elution with ethanol, solvent evaporation and

reconstitution with physiologic saline solution Injectable solutions of chemically and radiochemically pure compounds could be obtained. Overall radiochemical yields (non-decay corrected) were 34±5%, 53±6% and 21±5% for [I-**3**]$^-$, [I-**9**]$^-$ and [I-**14**]$^-$, respectively; radiochemical purity was above 95% in all cases at injection time.

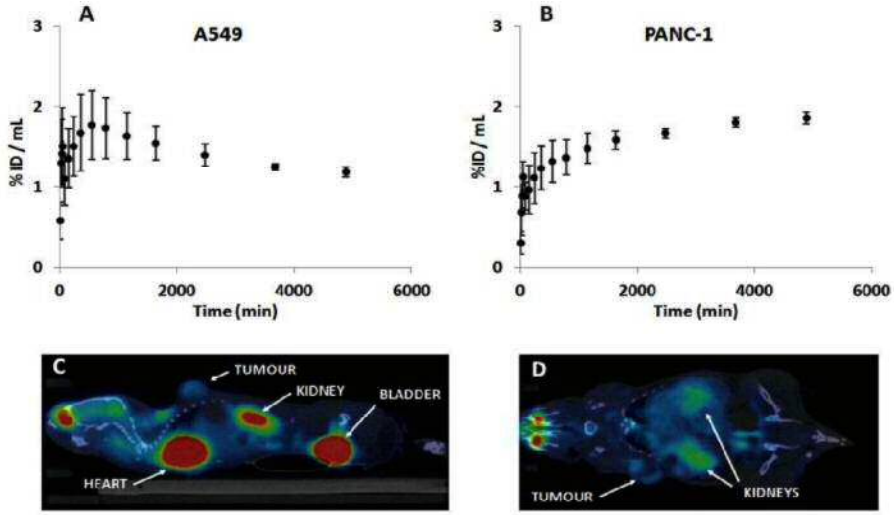

Figure 7.6. Biodistribution of [^{18}F]FDG in subcutaneous PANC-1 and A549 xenograft mouse model. Time-activity-curves in the tumor, expressed as the percentage of the injected dose per cm^3 of tissue are shown in (A) and (B). PET images obtained after administration of [^{18}F]FDG in mice bearing A549 (C) and PANC-1 (D) tumors.

Imaging studies were performed using two subcutaneous mouse tumour models: PANC-1 (human pancreatic carcinoma) and A549 (carcinomic human alveolar basal epithelial cell line), which were selected because of the high prevalence, morbidity and mortality associated to pancreatic ductal adenocarcinoma (PDAC) and non-small cell lung carcinoma (NSCLC).

The imaging studies were first conducted with [^{18}F]FDG, a glucose analogue in which the hydroxyl group at the 2-position is substituted by a ^{18}F atom. This tracer is widely used in the clinical diagnostic arena for the early diagnose of a wide variety of tumours, as well as for the evaluation of the response to treatment. The typical biodistribution pattern was observed (Figures 7.6 C and 7.6 D): high accumulation was detected in the kidneys and the bladder due to elimination mainly via urine, while significant uptake was also observed in the heart and the brain, organs which are known to consume a significant amount of glucose. For both models (PANC-1 and A549), the tumours could be clearly visualized on the images (Figure 7.6 C and D). As can be seen, the accumulation of [^{18}F]FDG in PANC-1 tumour follows a progressive increasing

trend, reaching values close to 2%ID/mL at long times (t>1h) after administration. For A549 tumour, after 10 minutes of injection of the radiotracer, a progressive decrease to values slightly above 1%ID/mL is observed. These results confirm the presence of metabolic activity in the tumours and suggest the correct perfusion of the tumour tissue.

The same animals were subsequently imaged using the newly developed labelled compounds ([^{124}I-**9**]$^-$ and [^{124}I-**14**]$^-$) in order to determine the accumulation in the tumour tissue over time and to get an indication of the potential of the compounds as potential BNCT drugs. Compound [^{124}I-**3**]$^-$ was also investigated as the control.

The three labelled compounds showed a similar biodistribution pattern, irrespective of the tumour model (Figure 7.7). The high accumulation in heart suggest the long residence time of the labelled species in the blood pool. A significant uptake was observed in the liver and the kidneys, suggesting a combined elimination *via* the urinary and the hepatobiliary routes. Accumulation of the radiotracers could also be detected in the lungs, with values always below 5% ID/mL. Unfortunately, accumulation in the tumour was relatively low, with values below 1%ID/g, irrespective of the compound and the tumour model.

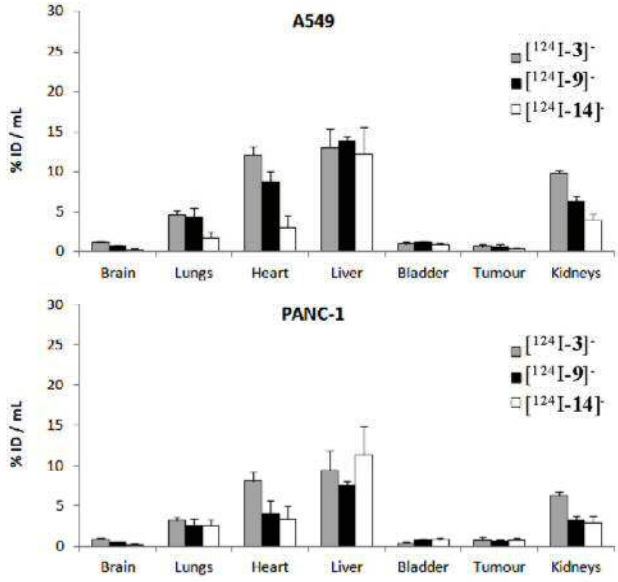

Figure 7.7. Biodistribution of [^{124}I-**3**], [^{124}I-**9**] and [^{124}I-**14**] in subcutaneous PANC-1 and A549 xenograft mouse model. Values are expressed as percentage of injected dose (%ID) per cm^3 of tissue and correspond to t=60 minutes after administration of the radiotracer.

7.1.2.- Dye-Sensitized Solar Cells (DSSC)

After the synthesis of the chlorinated oxidized and reduced derivatives ($[NMe_4][Cl_6$-**4**] and $Na_2[Cl_6$-**4**]), the preparation of DSSC devices with these complexes as electrolytes in cells and master plates was tested in collaboration with Dr. Valentina Mirruzzo from Prof. Aldo Di Carlo group at University of Rome.

As shown in section 4.3, in this thesis that follows others previous carried out in the group on a related electrochemistry subject, we have searched on the tuning of the scaffold $[M(C_2B_9H_{11})_2]^-$ to modify the $E_{1/2}$ in a controlled manner. Our first projects were dedicated to the $[Co(C_2B_9H_{11})_2]^-$ scaffold. With $[Co(C_2B_9H_7I_4)_2]^-$ we were able to lower $E_{1/2}$ by 1.2 V with respect to the pristine [**3**]$^-$. But it was still aprox 0.3 V more negative than the iodide/triodide couple. One of the hypotheses that we manage about the suitability of the I^-/I_3^- electrochemical couple for DSSC is that both components of the couple iodide triodide are negative and that it is very uncommon to find other couples with this situation. Halogenated derivatives of [**3**]$^-$ shall fulfill it.

Also, the scaffold $[M(C_2B_9H_{11})_2]^-$ allows to lower the $E_{1/2}$ potential values by moving from [**3**]$^-$ to [**4**]$^-$. Both Co and Fe metals are protected by a canopy of hydrogen atoms in the framework. This is also very unusual. As described in section 4.3, by adding an increasing number of iodine atoms covalently linked to the platform, the $E_{1/2}$ potential becomes more anodic. Thus [**4**]$^-$ has a $E_{1/2}$ potential of -0.78 compared to ferrocene. The [I-**4**]$^-$ is of -0.56; the [I_2-**4**]$^-$ of -0.35. The [I_4-**4**]$^-$ is of -0.29 and [I_8-**4**]$^-$ is +0.23 V, all referenced to ferrocene. We have described the compounds as the oxidized forms. This is why the oxidized forms are mononegative; the reduced ones have two negative charges and correspond to [**4**]$^{2-}$, [I-**4**]$^{2-}$, [I_2-**4**]$^{2-}$, [I_4-**4**]$^{2-}$ species, respectively. To notice is that the reduced forms are usually pink color, the oxidized ones are brownish/greenish.

In the case of chlorinated derivatives of [**4**]$^-$, the $E_{1/2}$ potentials are 0.00 V and +0.22 V for [Cl_6-**4**]$^-$ and [Cl_8-**4**]$^-$, respectively. As described in section 4.3, this slightly impure [Cl_6-**4**]$^-$ contains less than 10% of [Cl_5-**4**]$^-$ and less than 10% of [Cl_7-**4**]$^-$. They are so closely related that by column and preparative thin layer can't be separated, but as it can be seen from the Cyclic Voltammetry all compounds appear as a single compound.

Because its easy synthesis, we have been able to scale it up to produce around 1.8-2 g of each of these $[Cl_6\text{-}\mathbf{4}]^-$ and $[Cl_6\text{-}\mathbf{4}]^{2-}$ during this thesis. Both, the oxidized $[Cl_6\text{-}\mathbf{4}]^-$ and reduced $[Cl_6\text{-}\mathbf{4}]^{2-}$ forms of the hexachlorinated ferrabisdicarbollide are highly soluble in acetonitrile. Thus, they were very interested to be tested as electrolytes in the DSSC devices. It was required 198 mg of the oxidized form as sodium salt, $Na[Cl_6\text{-}\mathbf{4}]$, and 1980 mg of the reduced form $Na_2[Cl_6\text{-}\mathbf{4}]$ to be applied to electrolytes in DSSC devices.

For the preparation of the DSSC devices; the acetonitrile solutions of the oxidized $[Cl_6\text{-}\mathbf{4}]^-$ and reduced $[Cl_6\text{-}\mathbf{4}]^{2-}$ forms were used as electrolytes in a molar ratio between reduced and oxidized form of 10:1.

These complexes, $[Cl_6\text{-}\mathbf{4}]^-$ and $[Cl_6\text{-}\mathbf{4}]^{2-}$, were mixed either with guanidine thiocyante (GuSCN) and with 1-methylbenzimidazole (MeBzIm). 3-methoxypropionitrile (MPN) has a high boiling point and it was simply inserted alone inside the cell via vacuum back filling. In order to have a comparison, commercial available Dyesol's EL-HSE was also used. Dyesol's EL-HSE (High Stability Electrolyte) is a low toxicity liquid electrolyte based on I^-/I_3^- redox couple, dissolved in MPN. This is the "work horse" electrolyte system for long term stability testing. Outstanding stability has been achieved with EL-HSE in in-house tests (25,600 hours of continuous light soaking at 55-60°C,[93] and 3000 hours at 85°C.[94]

With these complexes $[Cl_6\text{-}\mathbf{4}]^-$ and $[Cl_6\text{-}\mathbf{4}]^{2-}$, GuSCN, MeBzIm and MPN, electrolytes has been formulated having the subsequent composition:

Final volume (mL)	Compound				Solvent
3	$Na_2[Cl_6\text{-}\mathbf{4}]$	$Na[Cl_6\text{-}\mathbf{4}]$	GuSCN	MeBzIm	MPN
Concentration (M)	0,2	0,02	0,1	0,2	

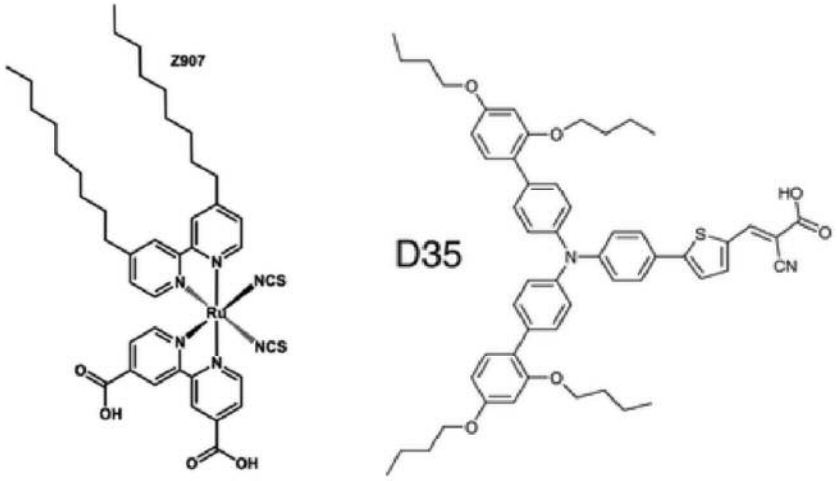

Figure 7.8. Formulae of the inorganic (Z907) and organic (D35) dyes.

The working photoanode of the DSSC device consisted in a film of TiO_2 with 6 micron of thickness, while the counter electrode was a Pt film. Both oxidized and reduced forms were deposited by automatic printing technique (screen printer) and then sintered.

Two different dyes were used: metallorganic Z907 (Ru complex) and organic dye D35 (Figure 7.8 displays the dyes formulae). All the devices were left still overnight.

Devices and measurements

Eight devices 3x1 were assembled, with a thermoplastic Bynel 60, in order to obtain a distance between electrodes around 40 μm. Four photoanodes were dipped in Z907 solution and the remaining four were dipped in D35 dye solution. In order to have a reasonable statistic, once device per dye was filled whit HSE electrolyte, and the other ones were filled with ferrabis(dicarbollide) electrolyte so the total number of cells was:

- ✓ 3 cells with Z907 dye and EL-HSE as electrolyte (Reference 1).
- ✓ 9 cells with Z907 dye and ferrabis(dicarbollide) as electrolyte.
- ✓ 3 cells with D35 dye and EL-HSE as electrolyte (Reference 2).
- ✓ 9 cells with D35 dye and ferrabis(dicarbollide) as electrolyte.

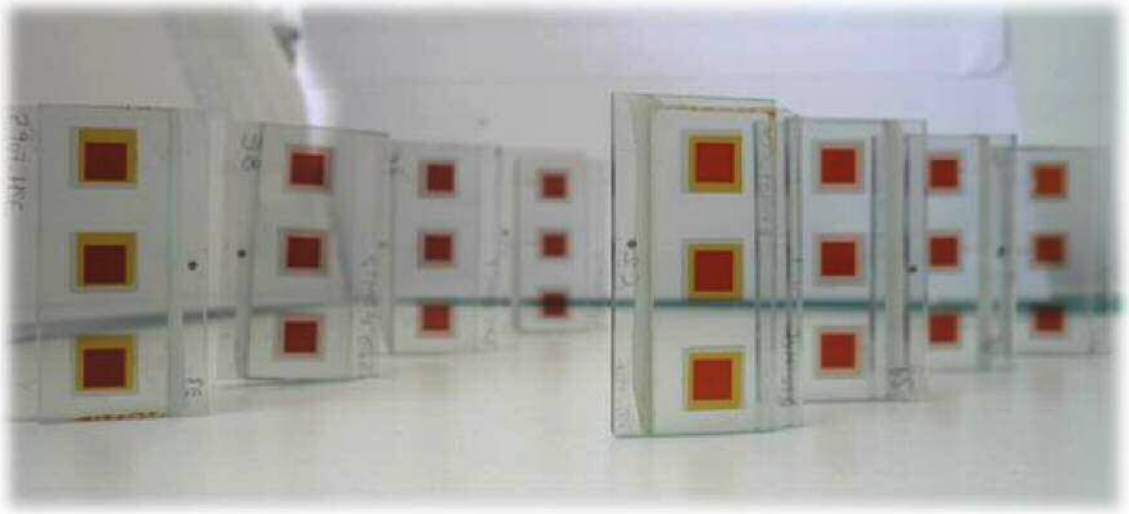

Figure 7.9. DSSC devices.

Measurements were carried out 24h after the assembling in a Class B Solar Simulator following the procedure: i) First Measurement; ii) Leave devices under Sun simulator (irradiation and temperature) for a 40 min period time; iii) Cooling down; iv) Second measurements.

Table 7.1 displays the first measurements of the total cells: 3 cells with Z907 dye and EL-HSE as electrolyte (Reference 1), 9 cells with Z907 dye and ferrabis(dicarbollide) as electrolyte, 3 cells with D35 dye and EL-HSE as electrolyte (Reference 2), 9 cells with D35 dye and ferrabis(dicarbollide) as electrolyte.

Sample	V_{oc} (Volt)	J_{sc} (mA/cm^2)	Fill Factor	Efficiency (%)	V_{oc} mean	J_{sc} mean	FF mean	Eff. mean
01-Z907-HSE_C1	0,715	11,82	58,56	4,948	0,704	12,325	58,130	5,039
01-Z907-HSE_C2	0,714	12,56	56,66	5,084				
01-Z907-HSE_C3	0,682	12,60	59,17	5,084				
02_Z907-ferrabis(dicarbollide)-1-C1	0,044	0,51	35,31	0,008	0,050	0,648	32,460	0,011
02-Z907-ferrabis(dicarbollide)-1-C2	0,047	0,64	32,25	0,0097				
02-Z907-ferrabis(dicarbollide)-1-C3	0,059	0,79	29,82	0,01399				
03-Z907-ferrabis(dicarbollide)-2-C1	0,055	0,68	27,49	0,01019	0,054	0,688	29,030	0,011
03-Z907-ferrabis(dicarbollide)-2-C2	0,055	0,71	28,71	0,01118				

03-Z907-ferrabis(dicarbollide)-2-C3	0,052	0,68	30,89	0,01099				
04-Z907-ferrabis(dicarbollide)-3-C1	0,051	0,65	34,18	0,01135	0,052	0,650	35,885	0,012
04-Z907-ferrabis(dicarbollide)-3-C2	0,054	0,64	34,54	0,01192				
04-Z907-ferrabis(dicarbollide)-3-C3	0,050	0,65	38,94	0,01274				
05-D35-HSE-C1	0,739	11,04	58,76	4,792	0,727	11,652	57,978	4,907
05-D35-HSE-C2	0,720	11,84	57,33	4,888				
05-D35-HSE-C3	0,722	12,07	57,84	5,04				
06-D35-ferrabis(dicarbollide)-1-C1	0,129	1,39	29,82	0,05344	0,136	1,409	29,521	0,057
06-D35-ferrabis(dicarbollide)-1-C2	0,137	1,41	29,66	0,05704				
06-D35-ferrabis(dicarbollide)-1-C3	0,142	1,43	29,09	0,0591				
07-D35-ferrabis(dicarbollide)-2-C1	0,138	1,59	28,50	0,06264	0,141	1,673	27,699	0,065
07-D35-ferrabis(dicarbollide)-2-C2	0,143	1,71	27,50	0,06701				
07-D35-ferrabis(dicarbollide)-2-C3	0,141	1,72	27,10	0,06565				
08-D35-ferrabis(dicarbollide)-3-C1	0,153	1,56	29,13	0,06938	0,153	1,672	28,375	0,073
08-D35-ferrabis(dicarbollide)-3-C2	0,148	1,65	27,94	0,06837				
08-D35-ferrabis(dicarbollide)-3-C3	0,159	1,81	28,06	0,08069				

Table 7.1. Results of the first measurement.

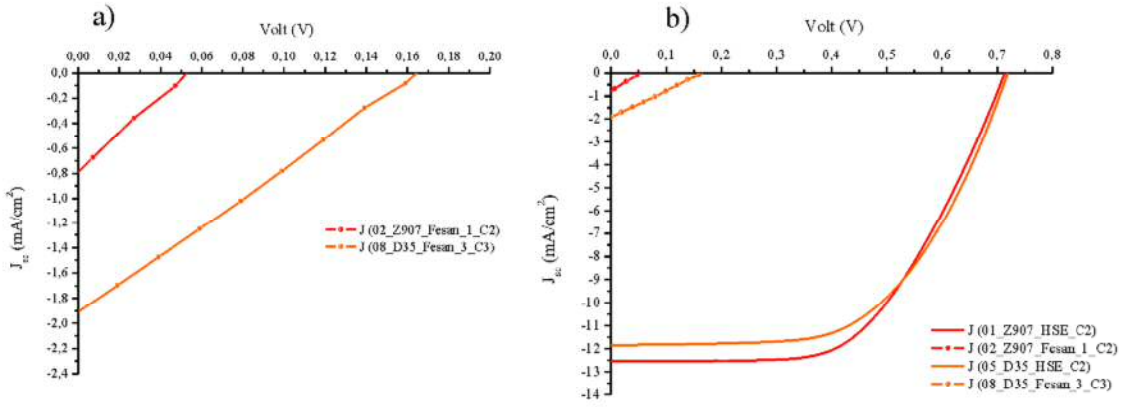

Figure 7.10. a) Graph J versus V of first measurements of two cells made with ferrabis(dicarbollide) complexes with the two different dyes (Z907 and D35). b) Graph of J versus V of the first measurements that compares HSE and ferrabis(dicarbollide) electrolytes with different dyes (Z907 and D35). Two cells are depicted as representatives.

Table 7.2 displays the second measurements of the total cells: 3 cells with Z907 dye and EL-HSE as electrolyte (Reference 1), 9 cells with Z907 dye and

ferrabis(dicarbollide) as electrolyte, 3 cells with D35 dye and EL-HSE as electrolyte (Reference 2), 9 cells with D35 dye and ferrabis(dicarbollide) as electrolyte.

Sample	V_{oc} (Volt)	J_{sc} (mA/cm^2)	Fill Factor	Efficiency (%)	V_{oc} mean	J_{sc} mean	FF mean	Eff. mean
01-Z907-HSE-C1	0,712	12,95	62,37	5,748	0,707	13,281	62,114	5,835
01-Z907-HSE-C2	0,717	13,27	62,50	5,948				
01-Z907-HSE-C3	0,693	13,62	61,48	5,808				
02-Z907-ferrabis(dicarbollide)-1-C1	0,515	0,69	37,87	0,13555	0,512	0,789	37,905	0,153
02-Z907-ferrabis(dicarbollide)-1-C2	0,505	0,81	38,09	0,15634				
02-Z907-ferrabis(dicarbollide)-1-C3	0,515	0,86	37,76	0,167				
03-Z907-ferrabis(dicarbollide)-2-C1	0,518	1,06	37,38	0,20549	0,492	1,050	33,976	0,177
03-Z907-ferrabis(dicarbollide)-2-C2	0,501	1,07	35,67	0,19122				
03-Z907-ferrabis(dicarbollide)-2-C3	0,456	1,02	28,88	0,13416				
04-Z907-ferrabis(dicarbollide)-3-C1	0,490	0,85	37,32	0,15511	0,462	0,878	34,639	0,142
04-Z907-ferrabis(dicarbollide)-3-C2	0,493	0,90	37,11	0,16418				
04-Z907-ferrabis(dicarbollide)-3-C3	0,403	0,89	29,48	0,10572				
05-D35-HSE-C1	0,755	11,30	59,09	5,04	0,741	11,659	58,153	5,023
05-D35-HSE-C2	0,733	11,86	57,20	4,976				
05-D35-HSE-C3	0,735	11,81	58,17	5,052				
06-D35-ferrabis(dicarbollide)-1-C1	0,423	0,44	37,40	0,06934	0,445	0,499	37,394	0,083
06-D35-ferrabis(dicarbollide)-1-C2	0,450	0,53	37,45	0,08861				
06-D35-ferrabis(dicarbollide)-1-C3	0,462	0,53	37,33	0,09172				
07-D35-ferrabis(dicarbollide)-2-C1	0,391	0,83	29,77	0,0967	0,401	0,839	30,061	0,101
07-D35-ferrabis(dicarbollide)-2-C2	0,410	0,87	30,14	0,1072				
07-D35-ferrabis(dicarbollide)-2-C3	0,402	0,82	30,27	0,09939				
08-D35-ferrabis(dicarbollide)-3-C1	0,443	0,67	35,99	0,107	0,444	0,608	32,959	0,090
08-D35-ferrabis(dicarbollide)-3-C2	0,429	0,68	34,86	0,10157				
08-D35-ferrabis(dicarbollide)-3-C3	0,459	0,47	28,03	0,0607				

Table 7.2. Results of the second measurements.

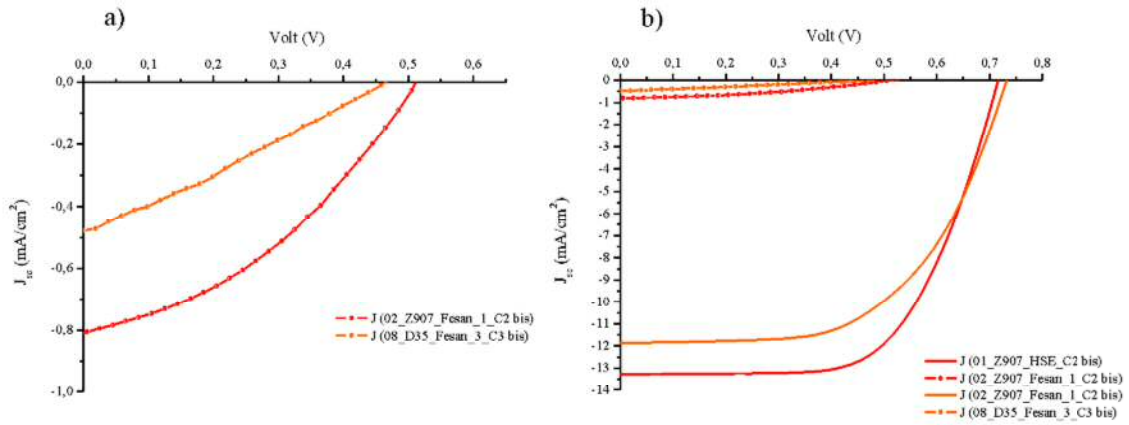

Figure 7.11. a) Graph J versus V of second measurements of two cells made with ferrabis(dicarbollide) complexes with the two different dyes (Z907 and D35). b) Graph of J versus V of the second measurements that compares HSE and ferrabisdi(carbollide) electrolytes with different dyes (Z907 and D35). Two cells are depicted as representatives.

As it is possible to notice, HSE electrolyte cells take advantage for all parameters; for what concerns ferrabis(dicarbollide) electrolytes, it seems clear a great increase in Voc after irradiation process for both dyes. It is less definite the current trend: considering all of the cells with ferrabis(dicarbollide), it can be seen that with Z907 dye there is an improvement of 33% in Jsc, but with D35 dye there is a loss of 57% in current.

The cells were left in shelf life for 10 days and new measurements were run after this period. The results are display in Table 7.3. After this shelf life period, there are no particular results or improvements that need to be pointed out. So, hexachlorinated ferrabis(dicarbollide) electrolytes have performances very low respect to common iodine based electrolyte. Maybe it is due to their steric hindrance, they suffer from ionic motility between the two cell electrodes.

Table 7.3 displays the measurements carried out after 10 days in shelf life of the total cells: 3 cells with Z907 dye and EL-HSE as electrolyte (Reference 1), 9 cells with Z907 dye and ferrabis(dicarbollide) as electrolyte, 3 cells with D35 dye and EL-HSE as electrolyte (Reference 2), 9 cells with D35 dye and ferrabis(dicarbollide) as electrolyte.

Sample	V_{oc} (Volt)	J_{sc} (mA/cm^2)	Fill Factor	Efficiency (%)	V_{oc} mean	J_{sc} mean	FF mean	Eff. mean
01-Z907-HSE-C1	0,761	11,18	65,90	5,604	0,747	11,895	64,750	5,747

01-Z907-HSE-C2	0,754	11,78	64,64	5,744				
01-Z907-HSE-C3	0,727	12,73	63,71	5,892				
02-Z907-ferrabis(dicarbollide)-1-C1	0,557	0,55	40,18	0,12393	0,541	0,472	39,348	0,101
02-Z907-ferrabis(dicarbollide)-1-C2	0,537	0,44	38,90	0,09153				
02-Z907-ferrabis(dicarbollide)-1-C3	0,530	0,42	38,96	0,08712				
03-Z907-ferrabis(dicarbollide)-2-C1	0,558	0,83	38,12	0,1761	0,536	0,582	37,479	0,118
03-Z907-ferrabis(dicarbollide)-2-C2	0,535	0,49	37,37	0,09709				
03-Z907-ferrabis(dicarbollide)-2-C3	0,515	0,43	36,95	0,08217				
04-Z907-ferrabis(dicarbollide)-3-C1	0,517	0,40	39,14	0,08082	0,536	0,390	38,867	0,081
04-Z907-ferrabis(dicarbollide)-3-C2	0,526	0,34	39,76	0,0702				
04-Z907-ferrabis(dicarbollide)-3-C3	0,565	0,43	37,71	0,09256				
05-D35-HSE-C1	0,781	10,29	62,03	4,984	0,770	10,983	62,124	5,248
05-D35-HSE-C2	0,756	11,62	61,17	5,376				
05-D35-HSE-C3	0,772	11,03	63,17	5,384				
06-D35-ferrabis(dicarbollide)-1-C1	0,462	0,42	38,73	0,0758	0,416	0,624	36,469	0,084
06-D35-ferrabis(dicarbollide)-1-C2	0,490	0,43	39,96	0,08438				
06-D35-ferrabis(dicarbollide)-1-C3	0,297	1,02	30,72	0,09285				
07-D35-ferrabis(dicarbollide)-2-C1	0,480	0,72	35,23	0,12152	0,472	0,612	36,484	0,105
07-D35-ferrabis(dicarbollide)-2-C2	0,469	0,48	37,18	0,08439				
07-D35-ferrabis(dicarbollide)-2-C3	0,467	0,63	37,04	0,10976				
08-D35-ferrabis(dicarbollide)-3-C1	0,505	0,38	38,49	0,07423	0,483	0,402	38,232	0,074
08-D35-ferrabis(dicarbollide)-3-C2	0,467	0,43	38,14	0,0759				
08-D35-ferrabis(dicarbollide)-3-C3	0,479	0,40	38,07	0,07258				

Table 7.3. Results of the measurements after 10 days in shelf life.

The results obtained with the DSSC study are perceived as contradictory: the range of $E_{½}$ potentials of the metallacarboranes studied are in the immediate vicinity of the I^-/I_3^- $E_{½}$ value, both members of the couple have negative charges, the electron transfer is produced presumably by an outer sphere process avoiding any structural modification, both members of the couple are stable in normal atmospheric conditions, they are compact molecules with dimensions in the range 1.2 x 0.6 nm, so no problem in the electron transfer process (ET); then why are so inefficient as electroactive electrolytes? Is there an electron recombination process?

It is known that appropriately substituted tris(bipyridine)cobalt(II) complexes (Co-bpy) have been found to function adequately as electron transfer mediators in DSSCs. However, their performance has so far not equaled that of more traditional mediators based on the I^-/I_3^- redox couple. It has also been shown that the equivalent Fe(II) complexes have not been functioning as electron transfer mediators in dye-sensitized solar cells. Then it may be something with the Fe.

The results in the work of this thesis have prompted to pursue research again on the $[Co(C_2B_9H_{11})_2]^-$ complex so to make its $E_{½}$ as anodic as possible or as similar to the I^-/I_3^- redox couple E½ value as possible.

It can be envisaged from the data reported in this thesis that 10-11 chloro atoms bonded to the parent cobaltabis(dicarbollide) could be enough to reach this target, so anions like $[Co(C_2B_9H_5Cl_6)_2]^-$ or $[Co(C_2B_9H_6Cl_5)_2]^-$ could perhaps do the job. Reaching such level of chlorination may be challenging. As written, the maximum chlorination number attained in this work is 8 Cl atoms as a major component. New synthetic procedures will have to be developed to reach such a challenging target, but it is expected that the efforts will be of value.

7.2.-Bibliography

[1] https://www.educacion.es/teseo/mostrarRef.do?ref=412938.
https://www.educacion.es/teseo/mostrarRef.do?ref=952995.

[2] A. Vaca, F. Teixidor, R. Sillanpää, R. Kivekäs, M. Arca, G. Barberà, C. Viñas, *Chem. Eur. J.*, **2009**, *15*, 9755.

[3] M. Mortimer, C. Knobler, M. F. Hawthorne, *Inorg. Chem.*, **1996**, *35*, 5750.

[4] (a) I. Rojo, F. Teixidor, C. Viñas, R. Kivekäs, R. Sillanpää, *Chem. Eur. J.*, **2003**, *9* 4311; (b) I. Rojo, F. Teixidor, R. Kivekäs, R. Sillanpää, C. Viñas, *Organometallics*, **2003**, 4642.

[5] (a) J. Yoo, J. W. Hwang Y. Do, *Inorg. Chem.*, **2001**, *40*, 568; (b) M. A. Fox, W.R.Gill, P. L. Herbertson, J. A. MacBride, K. Wade, *Polyhedron*, **1996**, *15*, 565; (c) M. A. Fox, J. A. MacBride, K. Wade, *Polyhedron*, **1997**, *16* (14), 2499.

[6] S.B. Yu, A.D. Watson, *Chem. Rev.*, **1999**, *99*, 2353.

[7] A. Pepiol, F. Teixidor, K. Saralidze, C. van der Marel, P. Willems, L. Voss, M. L. W. Knetsch, C. Viñas, L. H. Koole, *Biomaterials*, **2011**, *32*, 6389.

[8] M. F. Hawthorne, D. C. Young, T. D. Andrews, D. V. Howe, R. L. Pilling, A. D. Pitts, M. Reintjes, L. F. Warren, P. A. Wegner, *J. Am. Chem. Soc.*, **1968**, *90*, 879.

[9] A. Westcott, N. Whitford, M. J. Hardie, *Inorg. Chem.*, **2004**, *43*, 3663.

[10] L. A. Leites, *Chem. Rev.*, **1992**, *92*, 279.

[11] G. Barberà, C. Viñas, F. Teixidor, G. M. Rosair, A. J. Welch, *Dalton Trans.*, **2002**, 3647.

[12] M. A. Fox, A. K. Hughes, *Coord. Chem. Rev.*, **2004**, *248*, 457.

[13] Complexes in which a σ H-E bond (E = H, B, Si, C) acts as a two electron donor to the metal center are called σ complexes.

[14] (a) O. M. Yaghi, M. O'Keeffe, N. W. Ockwig, H. K. Chae, M. Eddaoudi, J. Kim, *Nature*, **2003**, *423*, 705; (b) R. N. Perutz, S. Sabo-Etienne, *Angew. Chem. Int. Ed.*, **2007**, *46*, 2578.

[15] M. Lein, *Coord. Chem. Rev.*, **2009**, *253*, 625.

[16] In order to distinguish between true agostic interactions and other weak electrostatic interactions distance ranges have been established. While the M–H distance is typically in the range of 1.8–2.3 Å, the M–H–C angles range between 90 and 140°.

[17] (a) F. Teixidor, A. M. Flores, C. Viñas, R. Kivekäs, R. Sillanpää, *Angew. Chem. Int. Ed.*, **1996**, *35*, 2251; (b) C. Viñas, R. Núñez, F. Teixidor, R. Kivekäs, R. Sillanpää, *Organometallics*, **1998**, *17*, 2376; (c) F. Teixidor, A. M. Flores, C. Viñas, R. Sillanpää, R. Kivekäs, *J. Am. Chem. Soc.*, **2000**, *122*, 1963; (d) F. Teixidor, A. M. Flores, C. Viñas, R. Kivekäs, R. Sillanpää, *Organometallics*, **1998**, *17*, 4675.

[18] (a) F. H. Allen, *Acta Crystallogr., Sect. B: Struct. Sci.*, **2002**, *58*, 380; (b) F. H. Allen, W. D. S. Motherwell, *Acta Crystallogr., Sect. B: Struct. Sci.*, **2002**, *58*, 407.

[19] O. Volkov, C. H. Hu, P. Paetzold, *Z. Anorg. Allg. Chem.*, **2005**, *631*, 1107.

[20] L. Cunha-Silva, M. J. Hardie, *Cryst. Eng. Comm.*, **2012**, *14*, 3367.

[21] P. Hurlburt, R. Miller, K. Abney, T. Foreman, R. Butcher, S. Kinkead, *Inorg. Chem.*, **1995**, *34*, 5215.

[22] L. Mátel, F. Macášek, P. Rajec, S. Heřmánek, J. Plešek, *Polyhedron*, **1982**, *1*, 511.

[23] D. A. Rudakov, V. L. Shirokii, V. A. Kniznikov, A. V. Bazhanov, E. I. Vecher, N. A. Maier, V. I. Potkin, A. N. Ryabtsev, P. V. Petrovskii, I. B. Sivaev, V. I. Bregadze, I. L. Eremenko, *Russ. Chem. Bull., Int. Ed.*, **2004**, 53, *11*, 2554.

[24] P. Farràs, C. Viñas, F. Teixidor, *J. Organomet. Chem.*, **2013**, *747*, 119.

[25] (a) P. Selucký, H. Baše, J. Plešek, S. Heřmánek, J. Rais, J. Czech. Patent 215 282, *Chem. Abstr.*, **1986**, *104*, 186637g; (b) J. Rais, P. Selucký, M. Kyrs, *J. Inorg. Nucl. Chem.*, **1976**, *38*, 1376.

[26] P. Matějíček, P. Cígler, K. Procházka, V. Král, *Langmuir*, **2006**, 22, *2*, 575.

[27] C. Viñas, M. Tarrés, P. González-Cardoso, P. Farràs, P. Bauduin, F. Teixidor, *Dalton Trans.*, **2014**, *43*, 5062.

[28] (a) J. F. Dozol, M. Dozol, R. M. Macias, *Macro. Chem.*, **2000**, *38*, 1; (b) G. Chevrot, R. Schurhammer, G. Wipff, *J. Phys. Chem. B.*, **2006**, *110*, 9488; (c) G. Chevrot, R. Schurhammer, G. Wipff, *Chem. Phys.*, **2007**, *9*, 1991.

[29] P. González-Cardoso, A. I. Stoica, P. Farràs, A. Pepiol, C. Viñas, F. Teixidor, *Chem. Eur. J.*, **2010**, *16*, 6660.

[30] (a) F. Teixidor, P. Angles, C. Viñas, *Inorg. Chem.*, **1999**, *38*, 3605; (b) J. Llop, C. Masalles, C. Viñas, F. Teixidor, R. Sillanpää, R. Kivekäs, *Dalton Trans.*, **2003**, *556*; (c) B. Grüner, J. Plešek, J. Báča, I. Císařová, J. F. Dozol, H. Rouquette, C. Viñas, P. Selucký, J. Rais, *New J. Chem.*, **2002**, *26*, 1519; (d) G. Barberà, C. Viñas, F. Teixidor A. J. Welch, G. M. Rosair, *J. Organomet. Chem.*, **2002**, *657*, 217; (e) F. Teixidor, J. Pedrajas, I. Rojo, C. Viñas, R. Kivekäs, R. Sillanpää, I. Sivaev, V. Bregadze, S. Sjöberg, *Organometallics*, **2003**, *22*, 3414; (f) P. Farràs, A. M. Cioran, V. Sicha, F. Teixidor, B. Stibr, B. Gruner, C. Viñas, *Inorg. Chem.*, **2009**, *48*, 8210; (g) P. Farràs, F. Teixidor, R. Sillanpää, C. Viñas, *Dalton Trans.*, **2010**, *39*, 1716.

[31] (a) S. S. Graham, P. A. Jelliss, *Inorg. Chim. Acta*, **2014**, *410*, 195; (b) P. A. Jelliss, S. S. Graham, A. Josipovic, S. Boyko, S. D. Minteer, V. Svoboda, *Polyhedron*, **2013**, *50*, 36; (c) A. B. Olejniczak, P. Mucha, B. Grüner, Z. J. Lesnikowski, *Organometallics*, **2007**, 26, 3272; (d) B. A. Wojtczak, A. Andrysiak, B. Grüner, Z. J. Lesnikowski, *Chem. Eur. J.*, **2008**, *14*, 10675.

[32] J. Plešek, B. Grüner, J. Macháček, I. Cisařova, J. Čáslavský, *J. Organomet. Chem.*, **2007**, *692*, 4801.

[33] (a) M. Brown, J. Plešek, K. Base, B. Stirb, *Mag. Reson. Chem.*, **1989**, *27*, 947; (b) X. L. R. Fontaine, N. N. Greenwood, J. D. Kennedy, K. Nestor, M. Thornton-Pett, S. Hemánek, T. Jelínek, B. Štíbr, *Dalton Trans.*, **1990**, 681.

[34] A. M. Cioran, F. Teixidor, Clara Viñas, *Dalton Trans.*, **2015**, *44*, 2809.

[35] T. O. Pennanen, J. Machácek, S. Taubert, J. Vaara, D. Hnyk, *Chem. Phys.*, **2010**, *12*, 7018.

[36] http://www.tdx.cat/handle/10803/117317.

[37] (a) S. H. Strauss, *Chem. Rev.*, **1993**, *93*, 927; (b) C. A. Reed, *Acc. Chem. Res.*, **1998**, *31*, 133; (c) C. A. Reed, K. C. Kim, R. D. Bolskar, L. J. Mueller, *Science*, **2000**, *289*, 101; (d) I. Krossing, I. Raabe, *Angew. Chem. Int. Ed.*, **2004**, *43*, 2066.

[38] (a) C. Masalles, S. Borrós, C. Viñas, F. Teixidor, *Adv. Mat.*, **2000**, *12*, 1199; (b) C. Masalles, J. Llop, C. Viñas, F. Teixidor, *Adv. Mat.*, **2002**, *14*, 826.

[39] (a) J. Plešek, *Chem. Rev.*, **1992**, *92*, 269; (b) I. B. Sivaev, V. I. Bregadze, *Collect. Czech. Chem. Commun.*, **1999**, *64*, 783; (c) R. N. Grimes, *J. Chem. Educ.*, **2004**, *81*, 658.

[40] P. Bauduin, S. Prevost, P. Farràs, F. Teixidor, O. Diat, T. Zemb, *Angew. Chem. Int. Ed.*, **2011**, *50*, 5298.

[41] D. Brusselle, P. Bauduin, L. Girard, A. Zaulet, C. Viñas, F. Teixidor, I. Ly, O. Diat, *Angew. Chem. Int. Ed.*, **2013**, *52*, 12114.

[42] In July 1st 2015, 71 crystal structures of pristine **[6]**$^-$ have been detected but the structure QOLVES (M. J. Hardie and C. L. Raston, *Chem. Commun.*, **2001**, *26*, 905) was chosen for this study.

[43] (a) R. H. Crabtree, P. E. M. Siegbahn, O. Eisenstein, A. L. Rheingold, T. F. Koetzle, *Acc. Chem. Res.*, **1996**, *29*, 348; (b) R. Custelcean, J. E. Jackson, *Angew. Chem. Int. Ed.*, **1999**, *38*, 1661; (c) P. C. Singh, G. N. Patwari, *Chem. Phys. Lett.*, **2006**, *419*, 265.

[44] J. Plešek, K. Base, F. Mares, F. Hanousek, B. Stibr, S. Heřmánek, *Collect. Czeck. Chem. Commun.* **1984**, *49*, 2776.

[45] P. Farràs, F. Teixidor, R. Kivekäs, R. Sillanpää, C. Viñas, B. Grüner, I. Cisarova, *Inorg. Chem.*, **2008**, *47(20)*, 9497.

[46] O. N. Kazheva, G. G. Alexandrov, A. V. Kravchenko, V. A. Starodub, I. A. Lobanova, I. B. Sivaev, V. I. Bregadze, L. V. Titov, L. I. Buravov, O. A. Dyachenko, *J. Organomet. Chem.*, **2009**, *694*, 2336.

[47] A. I. Stoica, C. Viñas, F. Teixidor, *Chem. Commun.*, **2009**, 4988.

[48] T. C. Li, A. M. Spokoyny, C. X. She, O. K. Farha, C. A. Mirkin, T. J. Marks, J. T. Hupp, *J. Am. Chem. Soc.*, **2010**, *132*, 4580.

[49] (a) E. Meggers, *Angew. Chem. Int. Ed.*, **2011**, *50*, 2442; (b) J. Rak, B. Dejlova, H. Lampova, R. Kaplanek, P. Matejicek, P. Cigler, V. Kral, *Mol. Pharm.*, **2013**, *10*, 1751.

[50] (a) M. Scholz, E. Hey-Hawkins, *Chem. Rev.*, **2011**, *111*, 11, 7035; (b) F. Issa, M. Kassiou, L. M. Rendina, *Chem. Rev.*, **2011**, *111*, 9, 5701; (c) E. L. Crossley, E. J. Ziolkowski, J. A. Coderre, L. M. Rendina, *Mini-Rev. Med. Chem.*, **2007**, *7*, 303.

[51] M. F. Hawthorne, J. I. Zink, J. M. Skelton, M. J. Bayer, C. Liu, E. Livshits, R. Baer, D. Neuhauser, *Science*, **2004**, *303*, 1849.

[52] (a) CSD consulted in July 7th, 2015; (b) For ConQuest program see: J. Bruno, J. C. Cole, P. R. Edgington, M. Kessler, C. F. Macrae, P. McCabe, J. Pearson, R. Taylor, *Acta Crystallogr.* B58, **2002**, 389.

[53] X. Yang, W. A. King, M. Sabat, T. J. Marks, *Organometallics*, **1993**, *12*, 4254.

[54] J. D. McKinney, F. S. McQuillan, H. Chen, T. A. Hamor, C. J. Jones, M. Slaski, G. H. Cross, C. J. Harding, *J. Organom. Chem.*, **1997**, *547*, 253.

[55] H. C. Kang, S. S. Lee, C. B. Knobler, M. F. Hawthorne, *Inorg. Chem.*, **1991**, *30*, 2024.

[56] O. N. Kazheva, G. G. Alexandrov, A. V. Kravchenko, V. A. Starodub, I. B. Sivaev, I. A. Lobanova, V. I. Bregadze, L. I. Buravov, O. A. Dyachenko, *J. Organom. Chem.*, **2007**, *692*, 5033.

[57] O. N. Kazheva, G. G. Alexandrov, A. V. Kravchenko, I. B. Sivaev, I. D. Kosenko, I. A. Lobanova, M. Kajňaková, L. I. Buravov, V. I. Bregadze, A. Feher, V. A. Starodub, O. A. Dyachenko, *Inorg. Chem. Commun.*, **2012**, *15*, 106.

[58] J. M. Forward, D. M. P. Mingos, A. V. Powell, *J. Organom. Chem.*, **1997**, *465*, 251.

[59] J. M. Forward, D. M. P. Mingos, T. E. Müller, D. J. Williams, Y. K. Yan, *J. Organom. Chem.*, **1994**, *467*, 207.

[60] L. Mátel, R. Cech, F. Macasek, S. Heřmánek, J. Plešek, *Radiochem. Radioanal. Lett.*, **1978**, *35*, 241.

[61] A. Pepiol, F. Teixidor, R. Sillanpää, M. Lupu, C. Viñas, *Angew. Chem. Int. Ed.*, **2011**, *50*(*52*), 12491.

[62] M. Lupu, A. Zaulet, F. Teixidor, E. Ruiz, C. Viñas, *Chem. Eur. J.*, **2015**, *21*, 6888.

[63] N. N. Greenwood, A. Earnshaw, in *Chemistry of the Elements* 2nd edn, Elsevier, **1997**.

[64] P. Farràs, E. J. Juárez-Pérez, M. Lepsik, F. Luque, R. Núñez, F. Teixidor, *Chem. Soc. Rev.*, **2012**, *41*, 3445.

[65] D. Olid, R. Núñez, C. Viñas, F. Teixidor, *Chem. Soc. Rev.*, **2013**, *42*, 3318.

[66] M. Corsini, F. Fabrizi de Biani, P. Zanello, *Coord. Chem. Rev.*, **2006**, *250*, 1351.

[67] F. Teixidor, C. Viñas, *Pure Appl. Chem.*, **2012**, *84*, 2457.

[68] (a) L. I. Zakharkin, V. A. Olshevskaya, E. V. Balagurova, P. V. Petrovskii, *Russ. J. Gen. Chem.*, **2000**, *70*, 550; (b) O. N. Kazheva, G. G. Aleksandrov, A. V. Kravchenko, V. A. Starodub, G. G. Zhigareva, I. B. Sivaev, V. I. Bregadze, L. I. Buravov, L. V. Titov, O. A. Dyachenko, *Russ. Chem. Bull.*, **2010**, *59*, 1137.

[69] A. A. Popov, I. E. Kareev, N. B. Shustova, E. B. Stukalin, S. F. Lebedkin, K. Seppelt, S. H. Strauss, O. V. Boltalina, L. Dunsch, *J. Am. Chem. Soc.*, **2007**, *129*, 11551.

[70] L. Pauling, *J. Am. Chem. Soc.*, **1932**, *54*, 3570.

[71] The polarization of *exo*-cluster bonds in carborane type architectures is not always intuitive. For a recent example and discussion of this situation, see A. El-Hellani, C. E. Kefalidis, F. S. Tham, L. Maron, V. Lavallo, *Organometallics*, **2013**, *32*, 6887.

[72] T. Daeneke, A. J. Mozer, T.-H. Kwon, N. W. Duffy, A. B. Holmes, U. Bach, L. Spiccia, *Energy Environ. Sci.*, **2012**, *5*, 7090.

[73] M. Tarrés, V. S. Arderiu, A. Zaulet, C. Viñas, F. Fabrizi de Biani, F. Teixidor, *Dalton Trans.*, **2015**, *44*, 11690.

[74] We have not identified other platforms that offer such a continuous and broad $E_{1/2}$ tuning.

[75] A. M. Spokoyny, T. C. Li, O. K. Farha, C. W. Machan, C. She, C. L. Stern, T. J. Marks, J. T. Hupp, C. A. Mirkin, *Angew. Chem. Int. Ed.*, **2010**, *49*, 5339.

[76] N. Ma, S. Li, L. Yan, Y. Qui, Z. Su, *Dalton Trans.*, **2014**, *43*, 5069.

[77] P. Sivy, A. Preisinger, O. Baumgartner, F. Valach, B. Koren, L. Mátel, *Acta Crystallogr. Sect. C-Cryst. Struct. Commun.*, **1986**, *42*, 30.

[78] P. Sivy, A. Preisinger, O. Baumgartner, F. Valach, B. Koren, L. Mátel, *Acta Crystallogr. Sect. C-Cryst. Struct. Commun.*, **1986**, *42*, 28.

[79] R. J. Mortimer, *Chem. Soc. Rev.*, **1997**, *26*, 147.

[80] (a) R. J. Mortimer, *Electrochim Acta*, **1999**, *44*, 2971; (b) M. Suzuki, N. D. Morris, T. E. Mallouk, *Chem. Commun.*, **2002**, 1534.

[81] (a) M. Tarrés, E. Canetta, C. Viñas, F. Teixidor, A. J. Harwood, *Chem. Commun.*, **2014**, *50*, 6700; (b) C. Verdià-Bàguena, A. Alcaraz, V. M. Aguilella, A. M. Cioran, S. Tachikawa, H. Nakamura, F. Teixidor, C. Viñas, *Chem. Commun.*, **2014**, *50*, 3370.

[82] (a) J. Q. Wang, C. X. Ren, L. H. Weng, G. X. Jin, *Chem. Commun.*, **2006**, 162; (b) K. J. Winberg, G. Barberà, L. Eriksson, F. Teixidor, V. Tolmachev, C. Viñas, S. Sjöberg, *J. Organom. Chem.*, **2003**, *680*, 188.

[83] (a) J. Plešek, S. Heřmánek, A. Franken, I. Cisarova, C. Nachtigal, *Collect. Czech. Chem. Commun.*, **1997**, *62*, 47; (b) P. Selucký, J. Plešek, J. Rais, M. Kyrs, L. Kadlecova, *J. Radioanal. Nucl. Chem.*, **1991**, *149*, 131.

[84] (a) I. B. Sivaev, Z. A. Starikova, S. Sjöberg, V. I. Bregadze, *J. Organom. Chem.*, **2002**, *649*, 1; (b) I. B. Sivaev, S. Sjöberg, V. I. Bregadze, *International Conference Organometallic Compounds - Materials of the Next Century*, Nizhny Novgorod, Russia, May 29-June 2, **2000**.

[85] J. Plešek, B. Grüner, S. Heřmánek, J. Báča, V. Mareček, J. Jänchenová, A. Lhotský, K. Holub, P. Selucký, J. Rais, I. Císařová, J. Čáslavský, *Polyhedron*, **2002**, *21*, 975.

[86] (a) B. Grüner, L. Mikulašek, J. Bača, I. Cisařova, V. Böhmer, C. Danila, M. M. Reinoso-Garcia, W. Verboom, D. N. Reinhoudt, A. Casnati, R. Ungaro, *Eur. J. Org. Chem.*, **2005**, 2022; (b) L. Mikulašek, B. Grüner, C. Danila, V. Böhmer, J. Časlavsky, P. Selucky, *Chem. Commun.*, **2006**, 4001.

[87] (a) A. B. Olejniczak, J. Plešek, O. Kříž, Z. J. Lesnikowski, *Angew. Chem. Int. Ed.*, **2003**, *42*, 5740; (b) Z. J. Lesnikowski, E. Paradowska, A. B. Olejniczak, M. Studzinska, P. Seekamp H Schüßler, D. Gabel, R. F. Schinazi, J. Plešek, *Bioorg. Med. Chem.*, **2005**, *13*, 4168; (c) A Olejniczak, J. Plešek, Z. J. Lesnikowski, *Chem. Eur. J.*, **2007**, *13*, 311.

[20 minutes after administration] animals were sacrificed by exsanguination.

[88] A. A. Semioshkin, I. B. Sivaev, V. I. Bregadze, *Dalton Trans.*, **2008**, 977.

[89] Z. Janousek, J. Plešek, S. Heřmánek, K. Base, L. J. Todd, W. F. Wright, *Collect. Czech. Chem. Commun.*, **1981**, *46*, 2818.

[90] (a) I. Bertini, C. Luchinat, G. Parigi, "Solution NMR of paramagnetic molecules: Applications to metallobiomolecules and models", *Elsevier Science* B.V. Amsterdam, The Nederlands, **2001**; (b) I. Bertini, K. S. McGreevy, G. Parigi, "NMR of biomolecules: Towards mechanistic systems biology", Wiely-VCH, **2012**.

[91] P. Jolliet-Riant, J. P. Tillement, *Fundam. Clin. Pharmacol.*, **1999**, *13(1)*, 16.

[92] LogD was calculated as log{[counts mL^{-1} (1-octanol)] / [counts mL^{-1} (buffer)]}.

[93] http://reginnovations.com/key-scientific-articles/long-term-stability-of-dye-solar-cells

[94] http://www.sciencedirect.com/science/article/pii/S0927024809004048; 1000 hours at 85°C.